Balloon-borne aerosol-cloud interaction studies (BACIS): Field

campaigns to understand and quantify aerosol effects on clouds

Varaha Ravi Kiran[1], Madineni Venkat Ratnam[1], Masatomo Fujiwara[2], Herman Russchenberg[3], Frank G Wienhold[4], Bomidi Lakshmi Madhavan[1], Mekalathur Roja Raman[5#], Renju Nandan[1], Sivan Thankamani Akhil Raj[1], Alladi Hemanth Kumar[1], Saginela Ravindra Babu[1$]

[1]National Atmospheric Research Laboratory (NARL), Gadanki, 517 112, India
[2]Faculty of Environmental Earth Science, Hokkaido University, Sapporo, 060-0810, Japan
[3]Department of Geoscience and Remote Sensing, Delft University of Technology, Delft, 2628CD, The Netherlands
[4]Institute of Atmospheric and Climate Science (IAC), Universitaetstrasse 16, Zurich, 8092, Switzerland
[5]Department of Physics, Sri Venkateswara University, Tirupati, 517 502, India
[#]now at Sathyabama Institute of Science and Technology, Chennai-600119, India
[$]now at Department of Atmospheric Sciences, National Central University, Taiwan

Correspondence to: Ravi Kiran. V (ravikiranv@narl.gov.in)

Abstract.

A better understanding of aerosol-cloud interaction processes is important to quantify the role of clouds and aerosols on the climate system. There have been significant efforts to explain the ways aerosols modulate cloud properties. However, from the observational point of view, it is indeed challenging to observe and/or verify some of these processes because no single instrument or platform is proven sufficient. Discrimination between aerosol and cloud is vital for the quantification of aerosol-cloud interaction. With this motivation, a set of observational field campaigns named Balloon-borne Aerosol Cloud Interaction Studies (BACIS) is proposed and conducted using balloon-borne in-situ measurements in addition to the ground-based (Lidars, MST radar, LAWP, MWR, Ceilometer) and space-borne (CALIPSO) remote sensing instruments from Gadanki (13.45o N, 79.2o E), India. So far, 15 campaigns have been conducted as a part of BACIS campaigns from 2017 to 2020. This paper presents the concept of the observational approach, lists the major objectives of the campaigns, describes the instruments deployed and discusses results from selected campaigns. Balloon-borne measurements of aerosol/cloud backscatter ratio and cloud particle count are qualitatively assessed using the range of corrected data from simultaneous observations of ground-based, space-borne lidars. Aerosol/cloud vertical profiles obtained in multi-instrumental observations are found reasonably agreeing. Apart from this, balloon-borne profiling is found to provide information on clouds missed by ground-based and/or space-borne lidars. A combination of the Compact Optical Backscatter AerosoL Detector (COBALD) and Cloud Particle Sensor (CPS) sonde is employed for the first time in this study to discriminate cloud and aerosol in an in-situ profile. A threshold value of COBALD colour index (CI) for ice clouds is found to be between 18 and 20 and CI values for coarse mode aerosol particles range between 11 and 15. Using the data from balloon measurements, the relationship between cloud and aerosol is quantified for the liquid clouds. A statistically significant slope (aerosol-cloud interaction index) of 0.77 found between aerosol backscatter and cloud particle count reveals the role of aerosol in the cloud activation process. In a nutshell, the results presented here demonstrate the observational approach to quantifying aerosol-cloud interactions.

1. Introduction

Understanding the fundamental process of aerosol-cloud interactions remains to be a challenging issue in the scientific community, already for more than three decades (Seinfeld et al., 2016). First-ever observational evidence from analysis of ship tracks using satellite imagery had opened up a wide scope for further research in this area (Coakley et al., 1987; Radke et al., 1989). Since then, efforts are underway using different observational and modelling techniques and lead to a significant development in the process-based understanding, quantification, and modelling (Abbott and Cronin, 2021; Fan et al., 2018; Haywood and Boucher, 2000; Koren et al., 2010; Lohmann, 2006; Lohmann and Feichter, 2004; Rosenfeld et al., 2008, 2014b). Despite all these efforts, radiative forcing estimates due to aerosol-cloud interactions both cloud

63 modification and further adjustments (ERFaci) still show large uncertainties (IPCC, 2021) in the range -0.3 to -1.7 W/m^2.

64 Apart from this, climate model simulations have uncertainties because parameterization schemes are inefficient in

65 representing the ways aerosols interact with clouds (Fan et al., 2016; Rosenfeld et al., 2014b; Seinfeld et al., 2016). At the

66 process level, various hypotheses have been proposed after the first indirect effect which was proposed almost four decades

67 ago (Twomey, 1977). All aerosol-cloud effects are found to act specifically to cloud type, background meteorological, and

68 dynamical conditions. For example, the invigoration effect is proposed for convective clouds (Rosenfeld et al., 2014a) under

69 the influence of updrafts. The first indirect effect (Twomey effect) and the second indirect effect (Albrecht effect) for liquid

70 clouds is influenced by mixing (Costantino and Bréon, 2010), turbulence, and entrainment (Jose et al., 2020; Schmidt et al.,

71 2015; Small et al., 2009). Although the first indirect effect is reasonably well understood, observational limitation poses

72 serious challenges in understanding and/or evaluating other hypotheses.

73   Among the various observational techniques that are currently available (ground-based, space-borne remote

74 sensing, and aircraft or unmanned aerial vehicle; UAV), none of the techniques alone has been proven self-sufficient in

75 aerosol-cloud interaction studies. For example, ground-based (and/or space-borne) lidars suffer serious attenuation and even

76 losses of observations due to the presence of optically thick cloud layers in the atmosphere. Thus, they may not be able to

77 represent the complete vertical structure of clouds and aerosols. Note that information on aerosol/cloud profiles is essential

78 for the estimation of their climate effects. Similarly, satellite data sets have shown distinct results and conclusions

79 (Grosvenor et al., 2018; Koren et al., 2010; McComiskey and Feingold, 2012) using different analytical methods for

80 example changing grid resolutions, etc. Besides this, in-situ measurements using aircraft and UAVs have been remarkable in

81 obtaining detailed information on the microphysics of cloud and aerosol (Corrigan et al., 2008; Girdwood et al., 2020, 2021;

82 Kulkarni et al., 2012; Mamali et al., 2018; Redemann et al., 2020; Weinzierl et al., 2017). However, there are serious

83 limitations concerning altitude coverage, the feasibility of conducting aircraft or UAV campaigns, and the overall cost

84 involved. Also, there is a chance that the aircraft perturb the atmosphere before it measures cloud/aerosol. Therefore, it is

85 essential to examine the combined information on aerosol/cloud, environmental parameters obtained simultaneously using

86 multi-instrumental techniques.

87   A classic paper by Feingold et al. (2003) first time quantified the 'Twomey effect' using ground-based remote

88   sensing instruments such as a microwave radiometer (MWR), cloud radar, and a Raman Lidar. In an intensive operations

89   program, Feingold et al. (2006) conducted airborne in-situ measurements for obtaining the cloud effective radius using an

90   aircraft in addition to the ground-based and space-borne remote sensing instruments. Pandithurai et al. (2009) also quantified

91   the 'Twomey effect' using a suite of ground-based remote sensing instruments (cloud radar, MWR, polarization Lidar) along

92   with the surface aerosol measurements (aerosol size distribution, scattering coefficient, and cloud condensation nuclei

93   concentration). Similarly, Sena et al. (2016) utilized 14 years of coincident observations from cloud radar and a Ceilometer

94   along with surface-reaching shortwave radiation measurements from the Atmospheric Radiation Measurement (ARM)

95   program over the Southern Great Plains, USA to investigate aerosol modifications on cloud macroscopic parameters and

96   radiative properties rather than cloud microphysical parameters. In addition to simultaneous measurements of cloud/aerosol,

97   concurrent measurements of thermodynamic and dynamic parameters of the atmosphere are also needed to thoroughly

98   understand the process of aerosol-cloud interactions. A step forward in this direction, McComiskey et al. (2009) used long-

99   term, statistically robust ground-based remote sensing data from Pt. Reyes, California, the USA to not only quantify the

100   'Twomey effect' but also examine the factors influencing the variability in aerosol indirect effects such as updraft velocity,

101   liquid water path, scale, and resolution of observations. Using a novel dual field of view Raman Lidar and a Doppler Lidar

102   technique, Schmidt et al. (2014) analyzed the data from Leipzig, Germany to explore linkages between aerosol, cloud

103   properties, and the influence of updrafts. Sarna and Russchenberg, (2016) used synergy of measurements from a Lidar

104   (Ceilometer), Radar (cloud radar) and a Radiometer (MWR) collected at ARM Mobile facility at Graciosa Island, the

105   Azores, Portugal, and the Cabaw Experimental Site for Atmospheric Research (CESAR) observatory, The Netherlands, to

106   not only quantify the aerosol indirect effect but also attempted to disentangle the effect of vertical wind (Sarna and

107   Russchenberg, 2017). All these studies contributed significantly to the knowledge on aerosol-cloud interactions but are based

108   on remote sensing techniques, limited to the low-level, warm, and non-precipitating clouds only.

109   Given the measurement limitations discussed above in ground-based multi-instrumental technique, a balloon-borne

110   in-situ measurement is suggested to be the complementary technique as balloons can pass through the cloud (during their

111   ascent/descent) representing the vertical structure of the cloud as well as aerosol below and above the cloud near

112 simultaneously (see Sect. 2 for details) without perturbing the atmosphere. Although there is less information and data on

113 balloon-based aerosol sampling artefacts than on conventional aircraft, information from balloon-borne in-situ measurements

114 in combination with the ground-based and/or space-borne remote sensing instruments will be of great help in constructing

115 the complete vertical profiles of aerosol, cloud, and further understanding the process of aerosol-cloud interactions. With this

116 in mind, a balloon-borne field campaign named BACIS (Balloon-borne Aerosol Cloud Interaction Studies) was initiated in

117 the year 2017 at National Atmospheric Research Laboratory (NARL), Gadanki (13.45^o N, 79.2^o E), India, with the multi-

118 instrumental approach.

119 Balloon-borne measurement of aerosol/cloud was first reported in Rosen and Kjome, 1991 using a backscatter

120 sonde developed by them. COBALD is similar to this but lightweight sonde (Brabec et al., 2012). Measurements of aerosol

121 size distribution in the stratosphere were carried out using an optical particle counter developed at Wyoming university

122 (Deshler et al., 2003). But Smith et al., 2019 developed a novel, low-cost, and lightweight open path configuration optical

123 particle counter, UCASS (Universal Cloud Aerosol Sampling System) for a wide range of particle size measurements

124 covering both aerosol and cloud. Kezoudi et al., 2021 and Mamali et al., 2018 used UCASS and reported balloon-borne in-

125 situ measurement of dust aerosol, compared UCASS with ground-based and airborne instruments. However, BACIS

126 campaigns are designed to understand and quantify aerosol-cloud interactions. For this, a combination of balloon-borne

127 sondes, COBALD and CPS is used for the first time to separate/discriminate aerosol and cloud in a profile. Note that

128 individually COBALD and CPS have been used in other studies (Brunamonti et al., 2018, 2020; Fujiwara et al., 2016a;

129 Hanumanthu et al., 2020; Inoue et al., 2021; Vernier et al., 2015, 2018).

130 The purpose of this manuscript is to introduce the motivation and objectives of the BACIS Campaigns for

131 quantifying aerosol-cloud interactions. In order to do this, we have discussed most related topics, such as the campaign

132 approach, sensors/instruments employed, analytical methods and comparison of balloon features. Results from selected

133 campaigns focus on discrimination of aerosol/cloud in a profile. Overall, the methods presented in this paper for the data

134 analysis/processing are novel. Using these methods aerosol-cloud interaction is estimated in liquid clouds.

135 **2. Instruments and methods**

136 **2.1. Balloon-borne sensors**

2.1.1. COBALD

The Compact Optical Backscatter AerosoL Detector (COBALD) deployed in BACIS campaigns is a lightweight (540 g) balloon-borne sonde developed in the group of Professor Thomas Peter at ETH Zurich, Switzerland. It is essentially a miniaturized version of the backscatter sonde developed by Rosen and Kjome (1991). A backscatter sonde is a balloon-borne sensor which measures the backscattered light from molecules, aerosol and clouds at two wavelengths in the vicinity of the sonde as it passes through the atmospheric column. The COBALD consists of two LED light sources of approximately 500 mW power emitting 455 nm (blue) and 940 nm (termed 'infrared') wavelengths, respectively (Brabec et al., 2012). The light emitted by the sonde illuminates the air in the vicinity, and backscattered light from an ensemble of particles is detected using a silicon photodetector. The emitted beam's divergence (with a full-width half-maximum of 4 degrees), detector field of view (of 6 degrees), and geometrical alignment of optics yields the reception of backscatter light from a distance of 0.5 m (overlapping distance) from the sonde. The region of up to 10 m from the instrument contributes to 90 % of the measured backscattering signal. The real-time backscatter data, in units of counts per second (cps, originating from the internal data treatment) is included in the radiosonde telemetry at a frequency of 1 Hz and sent to the ground station along with the pressure and temperature measurements. In the present case, we have used an iMet radiosonde (InterMet, USA). The COBALD sondes were usually operated for about 15 minutes at the surface (before launch) for thermal stabilization, sonde response is verified by cross-checking the LED brightness monitor signals with sonde specific reference values provided by the manufacturer. The sonde is launched when the monitor signal data at the surface is within ±15% of the reference value. COBALD sensor illuminates the air in the vicinity. Therefore does not require any flow to operate.

2.1.2. CPS

Cloud Particle Sensor (CPS) sonde is a lightweight balloon-borne sensor (~200 g) developed for the detection of cloud particle number and phase (Fujiwara et al., 2016). The latest version of the sonde (launched in the campaigns) is supplied by Meisei Electric Corporation, Japan, along with a Meisei RS-11G radiosonde (Kobayashi et al., 2019; RS-11G(R3) is the model with an interface for CPS). CPS primarily consists of a column (~1 cm x 1 cm in cross-section and ~12 cm in vertical length) for air passage, a diode laser (~790 nm, polarized), and two silicon photodetectors. Cloud particles entering the column due to the balloon ascent are illuminated by the laser. The scattered light from cloud particles is detected

162   by the photodetectors placed at an angle of 55° and 125° to the incident laser light. The detector at 125° comes with an

163   additional polarization plate positioned in front of it for the detection of cross-polarization whereas the detector at 55°

164   measures the intensity of plane-polarized scattered light. The intensities I55 and I125, for the detectors located at 55° and

165   125°, respectively, are provided in voltage. The minimum size of a water droplet that can be detected by CPS is found to be

166   2 µm (1 µm particles are undetected in laboratory experiments using various standard spherical particles) and I55 was found

167   to sometimes saturate (~7.5V) for particles ~80-140 µm (Appendix A of Fujiwara et al., 2016). Real-time data from CPS has

168   been transferred to the ground station through RS-11G (R3) radiosonde at a frequency of 1Hz. CPS data include the number

169   of particles counted in a sec, scatted light intensity (in Voltage) for the two detectors (I55 and I125), as well as particle signal

170   width for the first six particles for each second, and DC output voltage. The particle information is transmitted to the ground

171   station only for the first six particles for each second due to the limited downlink rate of RS-11G which is 25 byte s^{-1}. Before

172   launch, the sonde is tested by spraying water near to air passage column for particle detection. For CPS, the sample flow

173   depends on the balloon ascent rate. Fujiwara et al. 2016, (Appendix B) measured the flow rate within the duct of the CPS by

174   using hot-wire anemometers and estimated that the flow rate in the detection area is about 0.7 times the balloon ascent rate.

175   We used the value of 0.7 (of balloon ascent) for this paper. The flow inside the duct and the detection area would be more or

176   less turbulent, meaning that the flow has a minor component of a complicated function of time and space, but for example,

177   taking a sort of averaging e.g. for 5 seconds, 10 seconds, 1 minute, etc. would dump the impacts of such a turbulent

178   component.

179   **2.2. Remote sensing instruments**

180   **2.2.1. MPL/Ceilometer**

181   A Micro Pulse Lidar (MPL) was operated on 06th June and 8th July 2017 during the first two campaigns. Complete

182   technical details of MPL used in the campaign can be found in Cherian et al. (2014). A low energy (< 10 µj) green (532 nm)

183   pulsed laser of pulse width less than 10 ns was shot from MPL at a pulse repetition frequency of 2500 s^{-1}. A Cassegrain type

184   telescope of 150 mm diameter and a PMT have been deployed to collect the backscattered photons (co-polarized) from

185   particles and clouds in the atmosphere. The entire system is operated at a dwell time of 200 ns which would correspond to a

186   range resolution of 30 m. The return signals were collected for 1500 bins which correspond to the total range of 45 km. A

187 profile of backscattered photons was obtained for every 300 µs and all profiles collected were averaged for every one

188 minute. The telescope field of view and laser beam divergence coincide or overlap at above ~150 m. Using the data from

189 MPL (from Gadanki and the nearby location at Sri Venkateswara University, Tirupati, India (13.62^0 N, 79.41^0 E; ~35 km

190 from Gadanki), Ratnam et al. (2018) reported the presence of an elevated aerosol layer in the lower troposphere (~3 km)

191 during South-West Monsoon Season and discussed the possible causes for the formation and maintenance of this elevated

192 layer. The low-level jet (LLJ) between 2 and 3 km in the lower troposphere present during the southwest Monsoon causes

193 the formation of an elevated layer. In addition, the presence of shear between LLJ and tropical easterly jet (TEJ) maintains

194 the elevated layer restricting the upliftment of aerosol. Prasad et al. (2019) also used the same dataset to discuss nocturnal,

195 seasonal, and intra-annual variations in the tropospheric aerosol.

196 A Ceilometer (make from Vaisala, Finland) was used in the rest of the campaigns during non-available dates of

197 MPL. It is similar to an MPL but operates at a 910 nm wavelength and provides round-the-clock measurements of cloud

198 base heights, and boundary layer height apart from aerosol extinction under all weather conditions (Wiegner et al., 2014).

199 **2.2.2. Mie Lidar**

200 Mie lidar at Gadanki is a unique lidar system with capabilities to probe the atmosphere to higher altitudes (~30 km).

201 This lidar was operated in almost all the campaigns. A very high energy (600 mJ) pulsed laser with a pulse width of a few 7

202 ns and a pulse repetition frequency of 50 s^{-1} is operated at a wavelength of 532 nm. A 320 mm diameter Cassegrain type

203 telescope along with a couple of PMT has been used as a detection assembly to collect the co and cross-polarized return

204 signal. However, the co-polarization channel (only) is analysed in the present study. The data is stored at a dwell time of 2 µs

205 which corresponds to the range resolution of 300 m and the profiles collected were averaged every 250 sec (~ 4 min). The

206 data is considered to be reliable from an altitude of 3-4 km as the field of view of the Mie telescope and laser beam

207 divergence overlap at this height (Pandit et al., 2014). For the first time, sixteen years of Mie lidar data have been analysed to

208 determine the long-term climatology of tropical cirrus clouds (Pandit et al., 2015). Gupta et al. (2021) reported the long-term

209 observations of aerosol extinction profiles using a combination of MPL, Mie lidar, and a space-borne CALIPSO lidar.

210 **2.2.3. CALIPSO**

Cloud-Aerosol Lidar with Orthogonal Polarization (CALIOP) is the space-born lidar onboard the CALIPSO satellite (L'Ecuyer, 2011). CALIOP consists of two pulsed diode lasers operating at 532 and 1064 nm wavelengths with pulse energy of 110 mJ and a repetition rate of ~ 20 Hz. A Backscattered signal is collected by an avalanche photodiode (APD) at 1064 nm and photomultiplier tubes (PMT) at 532 nm. The signals at 532 nm are collected at both parallel and perpendicular to the plane of polarization of the outgoing beam, while for 1064 nm channel polarization is parallel only. The range resolution of the backscattered profile at 532 nm is 30 m for the altitude range from -0.5 to 8.2 km, 60 m for 8.2 to 20.2 km and 180 m for >20-30 km. Horizontal resolution is 0.33 km for -0.5 to 8.2 km and 1 km for 8.5-20.2 km. More details about CALIOP can be found in Winker et al. (2007).

2.2.4. MST Radar

The Indian MST radar located at Gadanki is a high-power coherent backscatter VHF (Very High Frequency) radar operating at 53MHz. A detailed description of MST radar can be found in Rao et al. (1995). Before the BACIS campaign, it has been upgraded to a fully active phased array with dedicated 1 kW solid-state transmitter-receiver units (total power of 1024 kW). This radar operates in Doppler Beam Swinging (DBS) mode to provide wind information covering the troposphere, lower stratosphere and mesosphere. Atmospheric scatterers are advected with the background air motions and the three-dimensional wind velocity vectors (zonal, meridional and vertical) can be directly deduced from the Doppler shifts of the radar echoes received in three independent beam directions. Note that these radars are the only means of getting direct vertical velocities presently and play a crucial role in the understanding of aerosol-cloud interaction processes. For the present study, data is obtained from five beam directions with 256 FFT (Fast Fourier Transform) points and coherent integrations, 4 incoherent integrations, Inter Pulse Period (IPP) of 160 ms, the pulse width of 8 μs coded covering the altitude region of 3 to 21 km with 150 m vertical resolution.

2.3. The observational concept of the BACIS Campaign

The schematic diagram shown in Figure 1 illustrates the observational approach. A meteorological balloon with specialized sondes such as COBALD (Brabec et al., 2012) and CPS (Fujiwara et al., 2016b) along with a radiosonde is launched ~10-30 minutes before CALIOP onboard Cloud-Aerosol Lidar and Infrared Pathfinder Satellite Observation (CALIPSO; Winker et al., 2007) (night time) overpass close by Gadanki. Ground-based remote sensing instruments at

236 NARL, Gadanki such as a Micro Pulse Lidar (MPL; Cherian et al., 2014) and/or a Ceilometer (Wiegner et al., 2014), a Mie

237 Lidar (subsequently referenced to as 'Mie'; Pandit et al., 2014), an Indian MST Radar (Rao et al., 1995) and/or a Lower

238 Atmospheric Wind Profiler (LAWP; Srinivasulu et al., 2012) are also operated before, during and after the launch. Other

239 observational facilities such as ambient aerosol instruments at the Indian Climate Observatory Network (ICON), NARL,

240 Gadanki and an MWR are operated during the launch period.

241   Table 1 lists the ensemble of instruments used in the campaign, their purpose and the physical quantity that can be

242 obtained from each instrument. Temporal variation of remote sensing data on the cloud and aerosol profiles is obtained from

243 ground-based (MPL/Mie) lidars. Spaceborne lidar (CALIPSO) also provides the same but for an along-track (roughly

244 meridional) distribution near the time of overpass over Gadanki. In-situ measurements of aerosol and cloud profiles along

245 with background meteorological parameters (temperature, relative humidity, wind speed and direction) are collected using

246 the specialized balloon sounding (COBALD and CPS). Temporal variation in wind components obtained from the ground-

247 based radars (MST Radar and/or LAWP) aids in entangling the effect of vertical winds and turbulence on aerosol-cloud

248 interactions. An MWR provides the cloud liquid water and relative humidity profiles, etc., useful to constrain the cloud water

249 content in a cloud layer to understand the aerosol influence on cloud properties. In addition to these measurements, surface

250 aerosol information obtained by the instrumentation available at the ICON observatory, NARL helps in understanding the

251 role of sources of aerosol from the surface. Altogether, near-simultaneous information on the aerosol, cloud and background

252 meteorological conditions obtained from the multi-instruments is aimed to understand the aerosol-cloud interactions.

253   Initially, when the experiment was being conceptualized, it was thought to conduct a launch once in one or two

254 months. However, due to the limited number stock of specialized sondes (available with us), it was decided to conduct

255 instead two pilot campaigns to demonstrate the concept proposed. A low-cost GPS/GSM-based tracker is used for the

256 recovery purpose. Two pilot campaigns were conducted in the early hours of 6 June and 8 July 2017. Table 2 lists the date

257 and time of all the balloon campaigns that have been conducted from Gadanki as a part of BACIS and the instruments

258 operated during the corresponding campaigns. As shown in Table 2, so far 15 launches have been conducted from the year

259 2017 to 2020. There was a maneuverer in CALIPSO orbit during September 2018 (CALIPSO track got departed from A-

260 Train to join C-Train. More details can be found at link https://atrain.nasa.gov/), followed by which we could not find

261 CALIPSO nighttime passage close by Gadanki. Also there was a limited availability of specialized Sondes, compatible

262 radiosondes, and GPS/GSM tracker assembly, among others. Because of these reasons, rest of the campaigns were

263 conducted on random dates. However, as seen in Table 2, we have managed to operate all the essential instruments proposed

264 in the observational approach during other campaigns. In particular, the campaigns in the year 2019 were conducted once a

265 month (March to June 2019) or for two months (July to December 2019).

266 Figure 2 shows the photographs taken at the balloon facility, NARL just before the launch during one of the

267 campaigns. The balloon payload with specialized sondes (COBALD, CPS) and radiosonde (iMet and RS-11G) is shown in

268 Fig. 2(a) and the prelaunch activities at the field are shown in Fig. 2(b). As shown in fig.2a, the ozonesonde at the centre

269 serves as the support for the balloon payload. COBALD sonde with a slight upward-looking angle is attached to one side of

270 the ozonesonde and the CPS on another side. Radiosonde (Meisei and iMet) connected to the remaining two sides. All the

271 sondes are tightly packed using adhesive tapes. At the base of the ozone sonde, a wide thick thermocol sheet is arranged to

272 protect the entire payload at the time of ground contact during descent. A couple of GPS/GSM based trackers are also

273 attached to the payload along with a power bank for safe recovery. The entire payload is hung to an inflated balloon with the

274 help of a nylon thread. The length of the thread between the inflated balloon and parachute is 5 m. Similarly, the length of

275 thread between the parachute and payload is 10 m. In this paper, CPS and COBALD data are shown at actual resolution (5

276 m). But in the estimation of the aerosol-cloud index sensor data is averaged over the thickness of the cloud which is about

277 300 m. Therefore, the sampling biases would be nullified.

278 With the observational approach described above, the following scientific issues/objectives are being pursued/realized:

279   i.   Demonstration of the potential of the multi-instrumental observational approach in obtaining the information on the

280   aerosol, cloud, and associated environmental parameters, such as 3D winds, relative humidity, and temperature

281   simultaneously.

282   ii. Comparison of balloon-borne in-situ measurements among the combination of spaceborne and/or ground-based

283   instruments.

284   iii. Discrimination of aerosol and cloud in a balloon sounding using the combined observations of COBALD and CPS

285   sondes.

286   iv. Verifying and quantification of aerosol-cloud interactions and understanding the influence of meteorological and

287   dynamical parameters.

288   v. Find out the differences, if any, in the estimates of aerosol-cloud interaction using multi-instruments and discuss the

289   possible reasons for discrepancies.

290   vi. Understanding of how the indirect effects of aerosols change radiative transfer through the atmosphere.

291   vii. Assessment of Weather and Climate model simulations using the multi-sensor data.

292   **2.4. Methods**

293   **2.4.1. COBALD data processing**

294   Backscattered light received by COBALD is contributed by molecules, aerosols and cloud particles in the

295   atmosphere. The molecular Rayleigh contribution to the raw signal (cps) is established during the post-processing of the data

296   using the simultaneous temperature and pressure recordings of the radiosonde. It serves to normalize the total signal in terms

297   of backscattering ratio (BSR) according to

298    $$BSR = \frac{\beta_{\text{total}}}{\beta_{\text{molecular}}}$$ (1)

299   Where β_{total} and $\beta_{\text{molecular}}$ are the backscatter coefficients corresponding to the contribution from particles plus molecules

300   and Molecules, respectively. The sole particle contribution is obtained by BSR-1, which expresses the ratio of particle

301   backscatter coefficient to the molecular one. The uncertainty in the COBALD BSR is estimated to be 1% and 5% at the

302   surface level and 10 km, respectively (Brabec et al., 2012; Vernier et al., 2015). The Color Index (CI), referring to the

303   particle backscatter only, is calculated from Equation 2.

304    $$CI = \frac{BSR_{940} - 1}{BSR_{455} - 1}$$ (2)

305   By definition, CI is an independent quantity of particle number concentration and is hence useful in interpreting the size of a

306   particle. For analysis, COBALD raw data is binned into 1 hPa pressure levels. This could minimize noise, and unwanted data

307   and smoothen the profile. Figure 3 shows a typical example of COBALD data collected during the second campaign (8 July

308   2017). BSR at 455 nm and 940 nm wavelength channels are represented by blue and red-coloured lines, respectively, while

309   CI (derived using Equation 2) is shown in the green-coloured line. From Fig. 3, a sharp increase in all parameters (BSR at

310   two channels, CI) found around 5 km associated with a thermal inversion (see temperature profile in Fig.3 in black colour)

311 may be attributed to the presence of a low-level cloud or elevated aerosol layer. Below ~5 km, the BSR profile indicates

312 tropospheric aerosol distribution. Within this altitude, BSR values around 2 km indicate boundary layer confinement. Note

313 no significant changes in CI within this 2 km height. Significant values in all parameters between 10 and 16 km are

314 indicative of multiple high-level cloud layers. In the rest of the campaigns, we have noticed that COBALD has captured

315 profile information that was missing in the lidar data.

316 **2.4.2. CPS data processing**

317   The phase of the cloud particle detected by CPS is determined using a quantity called degree of polarization (DOP)

318 given by the following relation:

319 $$DOP = \frac{I55 - I125}{I55 + I125}$$ (3)

320 Since the spherical particles (water droplets) do not provide significant voltage in the cross-polarization (I125 close to 0), the

321 DOP values for such particles would be close to 1. On the other hand, the DOP for non-spherical particles (for example ice

322 crystals) would take values between -1 and 1 randomly as I125 is non-zero and may or may not be greater than I55. Apart

323 from this, CPS can also detect the non-spherical particles in the lower troposphere whose DOP values may vary between -1

324 and 1.

325   The volume of the particle detection area within CPS is non-zero and estimated as ~0.5 cm^3 (see section 2.3 of

326 Fujiwara et al., 2016 for details). Therefore, when the particle number concentration is greater than ~2 cm^{-3}, more than one

327 particle would exist simultaneously in the detection area, resulting in particle overlap and multiple scattering and thus a

328 counting loss. The counting loss occurrence can be identified using a housekeeping parameter called 'particle signal width'

329 defined as the time taken for the detection of a single particle. A simple correction of particle count using the particle signal

330 width information is proposed by Fujiwara et al. (2016, see their section 2.3 for the details) using a factor 'f' which is

331 (particle signal width in ms)/(1 ms) as follows. The raw counts from a CPS are corrected for multiple scattering and overlap

332 effects using particle signal width data using Equation 4.

333 $$N_{corr} = N_{meas} \text{ x } 4f^3$$ (4)

334 Finally, the number of particles counted per second is converted to number concentration by assuming that the airflow at the

335 CPS detection area is 70% of the balloon ascent rate (see Appendices B and C of Fujiwara et al., 2016). The uncertainty of

336   the number concentration when the above correction to the particle count is made (i.e., for the case of $> \sim 2$ cm^{-3}) has not

337   been evaluated by Fujiwara et al., 2016. It would be safe to assume that the estimated number concentration is valid in the

338   representation of variations in the cloud property rather than magnitude.

339   CPS data were analyzed at their actual resolution of $\sim$ 5m. Figure 4a shows the corrected cloud particle (number)

340   count (based on eq. 4) for the same day as shown in Figure 3. Significant cloud particle count is found at around 5 km and

341   from above 10 to 16 km. The number of particles counted per second at 5 km turns out to be high suggesting the presence of

342   a dense (optically thick) layer of low-level cloud. The corresponding cloud particle number concentration (#/cm^3) also

343   represents (Fig. 4b) the cloud layers at the same altitudes. The DOP is estimated as per Equation 3. In Fig. 4c, DOP values

344   are found to be clustered in the region close to 1 at $\sim$5 km, indicating that the dense (low) cloud layer is a liquid cloud. On

345   the other hand, the DOP values are randomly distributed between -1 and 1 in the altitude region of >10 to 16 km, indicating

346   that these are ice clouds. In Fig. 4d and 4e, particle signal width is often greater than 1 ms and I55 is sometimes $\sim$7.5 V for

347   the ice cloud region between 11 and 14 km suggesting particle overlap and multiple scattering which might have led to

348   signal saturation. This portion of the profile is more vulnerable to the data correction which has been performed and shown

349   in Fig. 4a.

350   **2.4.3. Lidar data processing**

351   Though the backscattered data at very high altitudes (>30 km) are not significant, it is used as a background signal

352   for noise correction. Range corrected signal (RCS) from MPL/Mie is calculated from noise corrected backscattered signal

353   multiplied with range square. In general, the RCS indicates the intensity of light backscattered from molecules, aerosols and

354   clouds in the atmospheric column. However, inversion techniques are commonly applied to the RCS with an assumption of

355   lidar ratio (the ratio of extinction coefficient to backscattering coefficient) to obtain the profiles of total backscatter

356   coefficient, and extinction coefficient of cloud/aerosol separately. Ground-based lidar data were analyzed at their actual

357   vertical resolutions. However, CALIPSO data were interpolated and processed at every 30 m resolution. This information is

358   used in the discussion (sec 3.1).

359   **2.4.4. Estimation of saturation relative humidity**

360   Two dedicated radiosondes from iMet and Meisei were employed in the balloon campaigns for the measurement of

361   meteorological parameters (temperature, pressure, relative humidity, and horizontal winds with height) as well as to act as an

362   interface with specialized sondes COBALD and CPS, respectively. As mentioned, temperature and pressure profiles from

363   the radiosonde were used in the post-processing of the COBALD sonde to scale the signal to the molecular Rayleigh

364   scattering. In addition to this, radiosonde temperature, and relative humidity is useful in understanding the state of saturation

365   of water vapour in the column. By convention, relative humidity reported from radiosonde is always over the plane surface

366   of liquid water (because radiosonde relative humidity sensors are factory calibrated) even below 0^0C. This is because water

367   droplets may exist even below 0^0C and down to -30 to -40^0C (in the form of supercooled liquid) in the atmosphere.

368   Saturation relative humidity (SRH) is defined in Fujiwara et al. (2016) (see also Fujiwara et al., 2003) as the ratio of

369   saturation vapour pressure over the plane surface of ice (e_{si}) to water (e_{sl}) expressed in units of percentage can be a good

370   metric to describe the state of water vapour in the atmosphere such as sub-saturation, saturation and/or super-saturation in

371   particular at air temperatures below 0^0C (with respect to ice). In this study, both e_{sl} and e_{si} are calculated using Hyland and

372   Wexler formulation (see Appendix A of Murphy and Koop, 2005) by using radiosonde temperature data. For temperatures

373   warmer than 0^0C, water vapour saturation is indicated by 100% RH. For temperatures colder than 0^0C, water vapour is said

374   to be saturated if RH ~= SRH and super-saturated when RH > SRH. This information is used in the discussion (sec 3.2).

375   **2.4.5. Discrimination of cloud and aerosol in a balloon profile**

376   COBALD measurement always represents backscatter light from the combination of aerosol and cloud. Obtaining

377   information on aerosol (only) is not possible (for COBALD) in the presence of clouds, and the corresponding regions have to

378   be identified and rejected. This cloud clearing has been established previously for studies related to the UTLS region

379   (Vernier et al., 2015, 2018). Contrary, for cloud investigation, the COBALD was used in combination with the Cryogenic

380   Frost point Hygrometer (CFH) to identify supersaturation (with respect to ice) below, above and within the cirrus clouds to

381   improve the understanding of microphysical processes in cirrus clouds (Cirisan et al., 2014). This sonde in addition detected

382   volcanic aerosol tracers in the stratosphere (Vernier et al., 2020). The Asian Tropopause Aerosol Layer (ATAL) is a well-

383   documented phenomenon occurring in the UTLS region during the Summer Monsoon Season in South Asia. Vernier et al.

384   (2015) proposed two cloud clearing methods for discrimination of aerosol from cirrus clouds in the ATAL region using the

385 physical quantities Color Index (CI), relative humidity over ice (RHi) and backscatter ratio (BSR) at 940 or 532 nm (the

386 latter was interpolated from the 455 nm data for inter-comparison with CALIOP). In the presence of CFH data, the RHi

387 cloud-filtering approach classifies ATAL/UTLS aerosol layers by the criterion BSR (at 532 nm) < 1.3 and RHi < 70%. For

388 measurements of COBALD alone, the CI method indicates clouds with CI < 7 and BSR (at 940 nm) < 2.5. It was shown that

389 both methods effectively discriminate ATAL aerosol from upper tropospheric thin clouds. Brunamonti et al. (2018) also

390 applied the cloud clearing criteria (BSR at 940 nm < 2.5, CI < 7 and RHi < 70%) following Vernier et al. (2015) and found a

391 clear signal of enhanced BSR (at 455 nm) between 1.04 and 1.12 indicative of the aerosol population in the ATAL region.

392 However, it is noted that the methods proposed by Vernier et al. (2015) and Brunamonti et al., (2018) were developed for the

393 UTLS aerosol and their applicability to COBALD measurements of boundary layer and/or mid-tropospheric aerosol needs to

394 be validated.

395   In the present study, we made use of a CPS sonde in tandem with COBALD. As already mentioned, CPS is

396 sensitive to particles in the size range of >2 μm and hence detects cloud particles (both liquid droplets and ice crystals) and

397 sometimes coarse mode aerosol particles (such as dust) of these sizes. Fujiwara et al. (2016) have demonstrated in detail the

398 potential of a CPS sonde using balloon sounding carried out at mid-latitude (Japan) as well as tropical sites (Indonesia).

399 Narendra Reddy et al. (2018) used a CPS measurement from Gadanki to validate their method of retrieving cloud vertical

400 structures based on radiosonde measurements. Therefore, to better segregate the clouds from aerosols in the COBALD

401 measurements, CPS sonde has added advantage to the methods using simultaneous RH data described by Vernier et al.

402 (2015) and Brunamonti et al. (2018). This implies wherever the cloud is present in a profile, CPS identifies it (along with its

403 phase) and the corresponding COBALD particle backscatter data refers to the cloud. The rest of the particle signals in the

404 COBALD profile should correspond to aerosol. However, it may correspond to the (thin) cloud also which might have been

405 missed or undetected by a CPS. So identification of aerosol and cloud in an altitude profile is the key measurement of this

406 paper. The concept is illustrated in sec 3.2.

407 **2.4.6. Estimation of Aerosol-cloud-interaction Index**

408   Balloon data from all campaigns can be pooled to explore the aerosol-cloud relationship. For this purpose, a simple

409 scheme is developed to carry out the required computations. CPS profile data is looked for a cloud layer present in the

410   altitude regime of liquid or low-level clouds (below 5 km). As already discussed, CPS also identifies particles of non-

411   spherical nature. To separate cloud particles from non-spherical particles, the following conditions have been imposed on

412   various CPS measured parameters. Cloud particle count should be >10 #/s, cloud droplet number concentration >10^{-3}#/cc,

413   DOP>0.6, relative humidity >95% and temperature >0 degC. As there is a chance of randomly distributed data points in the

414   measurement column satisfying the above conditions, we considered only those points present continuously up to a thickness

415   minimum of 100 m (with at least one point for every 40 m). Further, COBALD data of blue backscatter 100m, 200m, 300m,

416   400m and 500m below the cloud base has been picked up separately (for the same profile) as a proxy of aerosol to check its

417   influence on the cloud above. As already mentioned, post-processed data of backscatter ratio from COBALD sonde

418   represents the contribution from both molecule and particle (cloud and/or aerosol). Hence, the particle backscatter ratio is

419   obtained by subtracting the backscatter ratio from one. To avoid high values of particle (blue) backscatter ratio possibly

420   originating from the interaction with high relative humidity usually expected near to cloud base (boundaries), we have

421   adopted two methods. First, high values of particle (blue) backscatter below the cloud base are removed if beyond a

422   threshold value of 3.15. The threshold is arrived at using a box plot (figure not shown) drawn for all the particle backscatter

423   data set (for sounding with clouds) from cloud base to 500 m below and found that 3.15 corresponds to the upper whisker

424   (Q3+1.5*(Q3-Q1)). Further, the particle backscatter data is corrected for relative humidity in case a statistically significant

425   (p-value <=0.05) and good correlation (>0.71) is found among relative humidity and particle backscatter ratio. A typical

426   example from the scheme is shown in Fig. 5 for the launch conducted on 01 November 2018 which depicts cloud layers,

427   blue particle backscatter ratio below the cloud along with shaded black dots (representative of aerosol backscatter ratio). The

428   scheme is applied to the balloon sounding and the results were discussed in sec 3.4.

429   Aerosol-cloud interaction can be quantified based on an index (ACI) using three methods discussed in Feingold et

430   al., 2003, 2006. ACI is defined as the slope of the linear fit between the logarithm of cloud proxies such as cloud optical

431   depth, cloud particle radius and cloud droplet number with the logarithm of aerosol proxy. ACI in this study has been

432   estimated using the equation (5).

433 $$ACI = \frac{dlogNc}{dlogBSRb} \qquad (5)$$

434 Where cloud droplet number count (Nc) is taken as cloud proxy whereas COBALD (blue) particle backscatter is (BSRb)

435 taken as aerosol proxy. It is to be noted that cloud particle number concentration is used here to represent cloud property

436 instead of droplet number concentration as the former is a direct measurement (of CPS). The slope of the linear fit between

437 the natural logarithm of Nc and BSRb indicates the magnitude of the aerosol-cloud interaction (ACI index) which should be

438 between 0 and 1 (Feingold et al., 2003). Note the condition shown in eq.5 is independent of the liquid water path as it

439 verifies/quantifies the aerosol activation process.

440 **2.4.7. Uncertainty in ACI estimation**

441 The uncertainty in ACI stems from both uncertainties in the COBALD backscatter ratio and CPS cloud particle

442 counts. The slope of the curve (linear fit of data on a log-log scale) can be written as a function of BSRb (blue backscatter

443 ratio) and Nc (cloud particle count) as,

444 $$ACI = f(BSRb, Nc) = \frac{LogNc - C}{LogBSRb} \qquad (6)$$

445 Where 'C' is the intercept of the curve. The partial derivative of *f(BSRb, Nc)* indicates uncertainty in ACI with respect to

446 uncertainty in individual parameters (Nc and BSRb). The combined uncertainty (UC) in ACI is given by the equation,

447 $$UC = \sqrt{\left(\frac{\partial f(BSRb,Nc)}{\partial BSRb}\right)^2 (uBSRb)^2 + \left(\frac{\partial f(BSRb,Nc)}{\partial Nc}\right)^2 (uNc)^2} \qquad (7)$$

448 Where *uBSRb* and *uNc* are individual uncertainties.

449 **3. Results**

450 **3.1. Comparison of balloon measurements**

451 It is important to know the performance of these sondes in comparison to other measurement techniques. Here, we

452 make use of data from two pilot campaigns to demonstrate the consistency of balloon-borne measurements with that of

453 ground-based and spaceborne remote-sensing instruments. As mentioned previously, the first two (pilot) campaigns have

454 been conducted in line with the proposed concept.

455 **3.1.1. Pilot campaign-1 (launch held on 06 June 2017 at 01:50 LT)**

456 The CALIPSO satellite overpass time for the first pilot campaign was around 02:00 LT on 06 June 2017 (starting

457 time of the track). The balloon was launched at 01:50 LT on the same day just before CALIPSO overpass time. Combined

458 measurements from specialized balloon-borne sondes and ground-based and space-borne lidars obtained during the first

459 launch of the campaign are shown in Figure 6.

460   The BSR from COBALD sonde at 455 nm (950 nm) is plotted in Fig. 6d as a blue (red) line. BSR from both

461 channels is referenced to the same x-axis scale. Similarly, cloud particle number concentration (dN, #/cc) from CPS sonde is

462 plotted as black dots (Fig.6e). On the other hand, range corrected signal (RCS) from ground-based lidars (Mie, MPL) is

463 averaged over a short period during the CALIPSO overpass and plotted in magenta (averaged from 01:50 to 02:00LT),

464 orange colour lines (averaged from 01:50 to 01:55 LT), respectively (Fig.6f). The total attenuated backscatter (km^{-1} sr^{-1})

465 from CALIPSO is also averaged for the profiles found nearest to the location and shown in an olive green colour line

466 (Fig.6f). The significant peaks in physical quantities being compared among the different measurements are representative of

467 responses from clouds and aerosols in the atmosphere. At this point of discussion, we have not distinguished their

468 contributions. The balloon drifts away from the launch location with time, therefore, it is also required to check the degree of

469 co-location of measurements with the lidars. To facilitate this, a portion of nocturnal variation (representing the balloon

470 launch duration) in range corrected signal from both Mie and MPL is shown in Fig. 6b and 6c, respectively. The CALIPSO

471 overpass track consisting of 166 profiles is also plotted as a function of longitude (Fig. 6a). For the sake of easy

472 identification of simultaneous lidar measurements, the balloon indices such as height and drift (radial distance from launch

473 location) are overplotted as a function of time on contour maps as shown in black and red-coloured lines, respectively (Fig.

474 6b and 6c).

475   Balloon-borne in-situ measurements from COBALD and CPS show significant peaks in the lower tropospheric

476 (below 4 km) and upper troposphere (between 13 and 17 km) at the same altitude regions. It can be seen from Fig. 6d and 6c,

477 that there is a good resemblance between the in-situ and MPL measurements in the lower tropospheric (below 4km). This is

478 because almost no change in the atmospheric conditions as the balloon took approximately 15 minutes to reach an altitude of

479 4 km with a radial distance of 5 km away from the launch location. Mie lidar information is not reliable for this altitude

480 region (below 4 km) as it is not in the overlapping region of the telescope viewing geometry and laser beam dispersion (see

481 section 2). CALIPSO signal also looks to be dispersed and noisy for this altitude region. This could be due to the attenuation

482 of the signal from the top side layers as seen in Fig. 6a at a longitude of 79.24^{o} E (nearest profiles longitude).

483   Next to this is the sharp peak seen in COBALD red channel at slightly below 9 km (Fig. 6d). This again can be seen

484   in Mie and MPL profiles also (Fig. 6b, 6c) but at 8.4 km (slightly below cloud detection height). However, it is to be noted

485   that these profiles are averaged for a short duration of time during the CALIPSO overpass. There is another peak in the Mie

486   lidar profiles at ~7.2 km (Fig. 6b), which is not seen in COBALD. It is approximately 45 min (around 02:45 LT) from the

487   time of launch when the balloon reached the altitude of ~9 km and 5.8 km away before detecting a sharp peak. As there is no

488   significant range corrected signal during this time and altitude in the ground-based lidar data (Fig. 6b and 6c), the sharp layer

489   detected by COBALD may be a localized cloud layer or a passing layer which might have ascended/descended. Exact

490   attribution can be made with a detailed study but it is beyond the scope of the current analysis.

491   Further, the balloon drift was within a 10 km range until 03:00 LT when it reached heights of ~12 km. This implies

492   weak horizontal winds and thus weakly associated wind drifts as well. Thereafter, the balloon started drifting rapidly due to

493   high wind speeds between 10 and 20 m/s. Both the in-situ measurements of COBALD and CPS show strong double peaks

494   from ~13-15.5 km and 16-16.5 km (Fig. 6d, e). Profiles from Mie, MPL and CALIPSO also showed similar peaks except for

495   MPL for which the upper side peak is missing (Fig. 6f). It may be once again noted that these profiles are averaged for a

496   short duration of time during the CALIPSO overpass the and return signal from MPL at high altitudes (~16 km) during the

497   same time suffered severely due to the presence of a mid-tropospheric cloud layer (at ~7 km) as seen in Fig. 6c. This is not

498   the case for the return signal from Mie Lidar as the power and energy of the Mie laser are relatively high (Fig. 6b). However,

499   strong double peak structures can be noticeable in the simultaneous observations of both ground-based lidars (Mie and MPL)

500   at similar heights during the time corresponding to the balloon altitude of 13 km (post 03:00 LT). Therefore, the same upper

501   tropospheric cloud layers detected in the ground, spaceborne and in-situ measurements suggest they are extended cloud

502   layers. Dynamical aspects of the southwest monsoon over the sub-continent refer to the presence of Tropical Easterly Jet

503   (TEJ) which is strong enough to swipe anvil clouds of mesoscale convective systems to thousands of kilometres

504   (Sathiyamoorthy et al., 2013).

505   **3.1.2. Pilot campaign -2 (launch held on 08 July 2017 at 01:35 LT)**

506   The starting time of the CALIPSO overpass track for the second pilot campaign was at 02:00 LT. The balloon was

507   launched at 01:35 LT nearly 30 minutes before the starting time of the CALIPSO overpass. Data from all the instruments are

508 plotted in Figure 7, which is prepared the same as Figure 6. MPL and Mie profiles were averaged from 01:50 to 02:00 LT

509 (close to the CALIPSO overpass time over Gadanki).

510   The observations from COBALD and CPS are matching reasonably well (Fig. 7d, e) as significant peaks were

511 found in the lower troposphere (0-5km) and upper troposphere (10-16 km). The profiles from spaceborne and ground-based

512 lidars (Fig. 7f) also show a similar response as in-situ measurements (both in the lower and upper troposphere) except that

513 lidar measurements exhibit additional peaks in the mid-troposphere (between 5 and 10 km). It is to be noted that profiles

514 from lidar measurements are averaged over a short period, as mentioned before.

515   Simultaneous observations from both the spaceborne (CALIPSO) and ground-based (Mie and MPL) lidars are

516 shown in Fig. 7 a, b &c respectively. Due to high wind speeds (10-20 m/s) the balloon drifted about 5 km away from the

517 launch site while crossing boundary layer height (~2km). The features found within the boundary layer as measured by in-

518 situ instruments (Fig. 7d) are in agreement with that of MPL measurements (Fig. 7c) for the same altitude region. Note that,

519 Mie lidar measurements are not reliable at these low altitudes and CALIPSO has not yet started passing by the launch site.

520 The balloon continued to drift away but with a reduced wind speed of 10 m/s. At around 4.3 and 4.7 km (10 km away from

521 the launch site), the balloon detected two layers (strong peaks). The time corresponding to this balloon height was around

522 01:50 LT and at this point, two layers can also be seen in both the ground-based lidars at the same altitudes (Fig. 7b and c)

523 indicating the presence of an extended layer (evident in both the in-situ and ground-based measurements). The layer at 4.7

524 km was also noticeable in the CALIPSO profile measurements (Fig. 7a). This is because the CALIPSO started coming close

525 to the site when the balloon was at this height and the CALIPSO profile corresponds to an average of (nearest) profiles at

526 around 79.32^0 E longitude (Fig. 7a). Further, the balloon started drifting towards the launch site until it reached a height of

527 ~7.5 km at a distance of ~13 km away. While moving towards the site, the balloon started detecting the layers starting from

528 11 km. The time corresponding to the balloon height of 11 km is around 02:45 LT and at this point of time simultaneous

529 MPL data show almost weak returns (Fig. 7c), whereas Mie lidar shows a better return signal (Fig. 7b) than MPL. In

530 continuation of this, the balloon started drifting further toward the site until it reached as close as ~3.5 km at a height of

531 ~12.5 km. Thereafter, it started moving rapidly away from the location with high wind speeds due to the characteristic of

532 TEJ. Multiple layers of clouds have been nicely captured by in-situ measurements from 11 km to ~ 16 km. However,

533 prominent lidar returns were not noticeable in the simultaneous observations of Mie and MPL. This is because of a strong

534 lower tropospheric cloud layer present at around 5 km limiting the detection of upper tropospheric cloud layers by both

535 ground-based lidars. However, all these layers were prominently captured in CALIPSO observations as it is top-down laser

536 probing.

537   In summary, the data from both pilot campaigns illustrate the limitations of the ground-based and/or spaceborne

538 lidars in detecting the complete cloud vertical structure. At the same time, in-situ data emphasize reasonable agreement of

539 the balloon-borne measurement with the ground-based as well as space-borne measurements and add to the remote sensing

540 techniques while detecting the missing portion of the cloud vertical structure.

541   The observational facilities at NARL are shown in figure 8. A typical example of high-resolution vertical wind

542 measurements obtained from MST Radar on 8 July 2017 is shown in Figure 9(f) and profiles of all the three-dimensional

543 winds averaged between 02:30 LT to 03:30 LT are shown in Figures 9(a)-(c) to compare the wind measurements. We also

544 superimpose the zonal and meridional winds in the respective panels obtained from radiosonde for comparison. Consistency

545 in the measured winds in these two independent techniques can be noticed. Since this campaign falls during the Indian

546 Summer Monsoon season, easterly wind velocities exceeding 50 m/s, which is called TEJ, can be noticed between 14-16 km

547 altitudes as a part of synoptic-scale systems (Fig. 9a). In addition, zonal winds are westerly, which is also part of a large-

548 scale monsoon system. These winds play a crucial role in bringing clouds and aerosol from far away sources. In general,

549 meridional winds are weaker and most southerly (Fig. 9b). Vertical winds show mostly updrafts, except in the UTLS region

550 where downdrafts are noticed (Fig. 9c) and similar features persist through this campaign (Fig.9f). Occasional patches of

551 updrafts and downdrafts can be noticed during the campaign, which is associated with monsoon convection. These vertical

552 winds act in the upliftment of aerosol and clouds. Enhanced SNR layers are also noticed (Fig. 9d) at a few altitudes mostly

553 related to large temperatures and water vapour gradients generally occur in the presence of clouds. Doppler width (Fig.9e)

554 shows higher values below the boundary layer and UTLS region suggesting active turbulence.

555 **3.2. Interpretation of aerosol and cloud features in a balloon profile**

556   To fulfill the primary objectives of the campaign, it is a priority to distinguish aerosol and cloud in a balloon-borne

557 in-situ profile. In connection with this, combined measurements of CPS and COBALD from a balloon sounding held on 27

558   June 2019 at 23:30 LT are interpreted as shown in Figure 10. This particular sounding is selected because it showcases all

559   the features that can be detectable by a CPS sonde in a profile such as liquid cloud, supercooled liquid cloud, ice cloud, and

560   non-spherical particle layers. INSAT3D brightness temperature shown in Figure S1 indicates the evolution of a localized

561   cloud system north of the observational site initiated a few hours before the launch and eventually spreading over the site.

562   To characterize the background conditions of the atmosphere, meteorological parameters such as relative humidity

563   (RH), and temperature (T) obtained from RS-11G radiosonde are plotted in Fig. 10a (wine red and blue colour lines). In Fig.

564   10a, SRH is also shown (in yellow colour). The SRH and RH can be read from the same top-X scale in wine red colour as

565   shown in Fig. 10a.

566   The CPS sonde usually features clouds that can be better identified with the information based on DOP, and

567   corresponding profiles of T, RH, and SRH. From Fig. 10d, DOP values close to 1 (from 0.6 to 1) are noticeable at different

568   altitude ranges in the profile viz., 3.5 to 5.5 km, 8.6 to 9 km and DOP values spread (-1 to 1) between 9 and 11 km. In the

569   altitude range from 3.5 to 5.5 km, CPS detected multiple liquid cloud layers, corresponding to the multiple layers of 100%

570   RH. However, the corresponding COBALD blue and red backscatter data points are limited (Fig. 10b). This is because

571   COBALD backscattered signals showed missing values due to saturation of photodiodes in the presence of thick liquid cloud

572   layers and that had to be removed during post-processing of data and are not discussed further.

573   The layer extending between 3.5 and 3.8 km (300 m thick) is observed with RH and T in the range 99-100% and 7-

574   8.7^{0}C, respectively, indicating saturation of water vapour with respect to liquid (RH~=SRH) which is conducive to the

575   formation of a (liquid) cloud. Further, the majority of droplet number concentrations in this liquid cloud layer range between

576   0.1 to 1 #/cm^{3}. A rough estimate of particle size information (water droplet or ice crystal) can be inferred from CPS voltage

577   data (I55). According to Fujiwara et al. (2016), I55 mostly lying below 1V suggests these droplets are sized ~2-13 µm.

578   Another liquid cloud layer extending from 4 to 4.4 km (400 m thick) is observed with vapour saturation over liquid (100%

579   RH) and temperatures from 3-6^{0}C. CPS shows that droplet number concentration peaks in the range 0.1-10 #/cm^{3} with the

580   highest in 0.1-1 #/cm^{3}. The intensity (I55) values (<1 V) indicate the majority of droplet sizes are ~2-13 µm. The third liquid

581   layer in the range of 3.5 to 5.5 km is observed between 5.1-5.5 km (400 m thick) with the highest droplet number

582   concentrations in the range of 0.1-10 #/cm^{3}, sized around 2-13 µm (I55<1 V). However, RH observations show 100%RH or

583   RH>SRH ie. water vapour super-saturated over ice at temperatures slightly below 0^0C (0 to -3^0C), suggesting that the cloud

584   layer may be composed of supercooled liquid droplets. Another clear supercooled cloud layer was detected between 8.6 and

585   9 km (400 m thick) with super-saturation of vapour over ice at 100%RH or RH>SRH and -21.5 to -23.5^0C temperatures. The

586   observed features of droplet number concentration and particle size are similar to those of the supercooled cloud found in the

587   lower atmosphere. The only difference that could be noticeable is in the distribution of DOP values as shown in Figure S2,

588   which indicates the tendency of droplets toward non-sphericity in the mid-tropospheric supercooled liquid cloud. COBALD

589   signals were found limited for all liquid/supercooled layers discussed above.

590   The topmost layer in the upper troposphere spreading from 9.5-11 km is an ice cloud layer as per its DOP values.

591   The temperatures within the cloud are found in the range of -22 to -40^0C. RH values are >SRH, suggesting the super-

592   saturation of vapour (over ice) within the ice cloud. The histogram of data for all the parameters obtained from COBALD

593   and CPS for this ice cloud layer (9-11 km) is shown in Figure 11. The number concentration of ice cloud particles (Fig. 11a)

594   lies between 0.01 to 10 #/cm^3 with a peak in the range of 0.1-1 #/cm^3. Non-sphericity of particles is seen by the wide

595   distribution of DOP values in the range -0.4 to 1 with the majority of them lying close to 0 (Fig. 11b). In particular, DOP

596   values close to 0 indicate (see section. 2) that both plane and cross-polarization intensities of scattered light (I55 and I125)

597   are comparable. This happens when both detectors get saturated due to a large number of small size particles and/or a few

598   large-sized ice particles or both. In support of this, the I55 values (Fig. 11c) are found to peak in the 7-8 V range (~7.5 V) for

599   such cases. Further, if saturation voltages are due to large size then they may correspond to ~80-140 µm or greater ice

600   particles (corresponding to I55 of ~7.5V), assuming that the results from laboratory experiments by Fujiwara et al. (2016)

601   using standard spherical particles can be applied for these ice clouds. Apart from this, the second peak in I55 noticed below

602   1V corresponds to ice particles roughly sized between 2 and 14 µm.

603   The COBALD BSR corresponding to this ice cloud is symmetrically distributed from 1-10 and 10-100 for blue

604   (Fig. 11d), red (Fig. 11e) wavelengths, respectively. However, there are some observations which are beyond 10(100) at blue

605   (red) wavelengths. Similarly, the CI for this cloud (Fig. 11f) is found mostly between 10 and 20 but for a few instances, it is

606   observed from 20 to 40. From the definition (see section 2), the CI is independent of the number concentration hence it can

607   be used as an indicator of the mode radius of particles. With the assumption of the single-mode log-normal size distribution

608   of spherical aerosol/cloud particles, Mie calculations show CI is 4-10 for small particles of mode radius up to 1-2 µm and 14-

609   20 for large particles of 2-20 µm. CI converges to around 20 as a geometric limit for very large particles of mode radius >

610   ~50 µm. However, CI can have values >20 at mode radius 2-20 µm as CI is a non-monotonous function of mode radius and

611   exhibits Mie oscillations (due to variations of scattering efficiencies with size parameter). The amplitude and frequencies of

612   Mie oscillations depend on the width of the log-normal size distribution assumed. At a width higher than say 2 (representing

613   polydisperse aerosol populations), these oscillations are mitigated and lead to a monotonous dependency of CI and mode

614   radius. For stratospheric aerosols in the size range of 0.02-0.4 µm, the CI is found to be in the range of 5-7 (Rosen and

615   Kjome, 1991). This is because stratospheric aerosols exhibit size distributions with narrow standard deviations. Aerosol size

616   distributions in the UTLS region may also be assumed as log-normal (similar to stratospheric aerosols) hence the criteria

617   CI<7 might have suited for cloud filtering in the ATAL region (see Section 2). For the present case of the ice cloud layer (9-

618   11km) discussed above, CPS indicates the presence of small (2-14 µm) and very large ice particles (>80 µm). So, the

619   standard deviation of log-normal size distribution in the cloud layer of large particle mode must be wider. Therefore, Mie

620   oscillations may be expected to be at a minimum. Probably because of this, the majority of CI values for the cloud layer are

621   found between 15 and 20, which may correspond to a mode radius of > ~50 µm (geometric limit). It may also be concluded

622   that the CI of 20-40 (with very few values >30) corresponds to small particles of mode radius > 2-20 µm (due to Mie

623   oscillations). COBALD size interpretations (based on CI) are in support of CPS-based size interpretations. Since the majority

624   of CI falls between 15 and 20, the I55 of ~7.5V in CPS would have been caused by large size particles.

625   In the lower troposphere up to 2 km where water vapour is well sub-saturated (50-70 %RH), CPS also shows

626   particle signals (Fig. 10c). The DOP values range from -0.4 to 1 but with lower number concentrations (0.001-0.01 #/cm^3)

627   and less than 1 V of backscatter intensity (I55), indicating these particles as non-spherical in shape similar to the ice cloud

628   particles. Since it is not possible to have ice cloud particles at these lower altitudes in dry conditions (RH<70%), it may be

629   possible that these particles are coarse mode non-spherical aerosol particles. COBALD observations indicate a CI of 11-12.

630   Thus, both the COBALD and CPS observations indicate aerosol may be of size ~2-5 µm. To investigate the possible origin

631   of these coarse mode aerosol particles, Hysplit 7-day back trajectories for 5 days before and after the date of launch are

632   calculated and shown in Figure S3 (in different colour lines). These Hysplit back trajectories (Stein et al., 2015) indicate the

633   air parcel pathways ending at every 1 km altitude from 1 to 5 km over Gadanki at the time of balloon launch (18 UTC). It

634   can be seen (from Fig. S3) that, the air masses originated from the Indian Ocean passing through the Arabian Sea before

635   reaching the Gadanki location for heights of 1 to 3 km. Therefore, the air masses were of marine origin, and the particles

636   were possibly coarse-mode water-soluble particles (such as sea salt) which can grow hygroscopically due to the availability

637   of moisture over the Ocean surface (Mishra et al., 2010; Ratnam et al., 2018). The rainwater chemical analysis reported by

638   Jain et al. (2019) at Gadanki supports this conclusion as they found dominance of water-soluble ions during the southwest

639   monsoon (June to September). Above 3 km altitude, the air masses are coming from the Saharan desert region (within 7

640   days) which may bring non-spherical coarse mode dust particles to the launch location (Mishra et al., 2010). Thus, in the

641   case of lower tropospheric coarse mode aerosol (water-soluble aerosol particles), the CI can be >7 at RH<70%.

642   In the altitudes of 6-8.5 km (Fig. 10), CPS has detected no cloud. However, COBALD data shows, that CI values

643   ranging from 3-8 in the altitude range of 6-7 km and 3-12 in the altitude range of 7-8.5 km may indicate the presence of

644   aerosol particles undetectable by a CPS (i.e., of sizes <2 μm). RH values indicate sub-saturated conditions throughout this

645   altitude region. However, between 7 and 8.5 km, RH increases and becomes greater than the ice saturation RH values

646   (saturation with ice). Corresponding to this RH change, CI, as well as red channel BSR, is also found to increase. This

647   suggests the growth of small aerosol particles under high humidity conditions until the RH approaches ice saturation where

648   supercooled liquid droplets are observed (8.6-9 km) in CPS whose features have been discussed already. Since the COBALD

649   CI values are mostly <10 in this altitude range, the majority of particles detected might be sized up to 1-2 μm.

650   **3.3. Statistics on COBALD colour index**

651   To generalize the optical properties specific to aerosol and cloud, combined data from COBALD and CPS (from

652   multiple launches) has been investigated in detail. The liquid/supercooled cloud, ice cloud and non-spherical particle layer

653   depth are carefully identified with the help of DOP data from CPS (discussed in Section 2). The corresponding data of

654   temperature, relative humidity, BSR, CI, and peak particle number concentration have been picked up for estimating

655   statistics. Further, threshold values of COBALD parameters were tried to identify for the said categories of aerosol and cloud

656   cases. Among 15 balloon soundings, those soundings were considered where CPS detected cloud particles and both blue and

657 red channel data are not missing from COBALD. With these conditions, 8 balloon soundings were identified for estimating

658 statistics.

659   Table 3 shows the mean (median) values of CI and other parameters corresponding to the ice cloud layers from 7

660 launches. Fig. 12(a) shows the complete statistics of CI in the form of a box plot for the same ice cloud layers. Fig. 12(b)

661 shows a histogram of CI from each campaign indicated by different colours. From Table 3, ice clouds are seen above 9 km

662 with temperatures colder than -20^{0}C. For example, an ice cloud layer was found between 9.3 to 16 km on 30 April 2019 with

663 temperatures in the range of -22 to -79^{0}C, RH close to SRH and mean (median) value of CI is 19.4 (19.3), BSR is 16.4 (8.6)

664 at 455 nm, 302 (147) at 940 nm, peak droplet concentration is in the range 10^{-1} to 1#/cc. Similarly, from Table 3, the range of

665 mean (median) values of BSR is noticed to be from 1.6 (1.4) to 17.2 (17.5) and 12.2 (8.7) to 318 (313) at 455 and 940 nm,

666 respectively. Therefore, it is difficult to arrive at threshold values of BSR for ice clouds based on Table 3. This may be partly

667 because BSR depends not only on the particle number concentration but also the size. However, it is interesting to note

668 (except for a few cases in Table 3) that BSR data of ice clouds (at both channels) tend to be greater for densely populated

669 clouds. On the other hand, the difference between mean and median values of CI is not large, thus not much variance in CI

670 within the ice cloud. It is also clear from Table 3 and Fig. 12(a) that about 90-95 percentile of CI values of ice clouds are

671 above 15 and below 25 with mean/median values in the range 18-20. The same is also seen in the histogram of CI shown

672 (Fig. 12b) in different colours for different sounding dates where a greater number of points in a sounding are lying close to

673 20. Therefore, it may be concluded that the mean value of CI of ice clouds would be between 18 and 20.

674   The data from 8 soundings are also analysed for CI (and other parameters) of liquid clouds. However, it is noted

675 that liquid clouds were not observed as often as ice clouds in the balloon data. In the second campaign (8 July 2017) a liquid

676 cloud layer was observed at altitudes from 4.7 to 4.86 km (160 m) with RH>SRH, temperatures in the range of -0.4 to -

677 1.65^{0}C. The mean value of CI corresponding to this liquid cloud layer is very high around 50. Similarly, another liquid cloud

678 layer was observed in the fourth campaign (01 Nov. 2018) in the altitude range of 2-2.3 km (300 m). The corresponding CI

679 values are high and above 100 (up to 200). A couple of thin supercooled liquid cloud layers were also identified on the same

680 sounding between 6.1-6.17 km (7 m) and 6.6-6.8 km (200 m). The corresponding CI values are found with mean (median)

681 values of 19.5 (19.4) and 32.6 (32.8), respectively. Apart from this, a strong boundary layer (liquid) cloud layer was

682   observed on 23 Mar. 2019 (fifth campaign) between 0.9 and 1.2 km (300 m). The corresponding CI of liquid cloud was

683   found to be high with mean, and median values of 60-80. From the above discussion (including the liquid cloud cases not

684   discussed above), it is noticed that the CI for liquid clouds is high. The difference in CI values of liquid clouds can be

685   attributed to the thickness of the cloud, and the density and droplet size of liquid clouds.

686   Non-spherical large dust aerosol particles were identified by DOP values from CPS in the lower troposphere where

687   RH is far less than 100%. Statistics on COBLAD CI (and other parameters) for these non-spherical particle cases are

688   presented in Table 4 using the data from 8 soundings. For example, a non-spherical particle layer was found between 0.5 and

689   2.5 km altitudes on 06 June 2017 with temperatures in the range of 15.5 to 27.6^0C and relative humidity is dry from 63.5 to

690   81.3%. The mean (median) value of CI corresponding to this non-spherical particle layer is 12.3 (12.5), BSR is 1.45 (1.4) at

691   455 nm, 6.5(6) at 940 nm and peak particle concentration is between 10^{-3} and 10^{-1} #/cm^3. The peak particle concentration of

692   all non-spherical layers is found to be in the same range and hence not shown. From Table 4, it can be noticed that the non-

693   spherical particle (aerosol) layer is found from the near-surface to the 5 km altitude depending on the month or season.

694   During the monsoon season (font in blue colour in Table 4), non-spherical particle layers were observed mostly from the

695   near-surface (500m) to 2.5 km whereas during pre-monsoon (font in wine red colour) it is found from 0.5 up to 5 km. The

696   reason for the difference in layer thickness among seasons may be attributed to the mixing within the lower troposphere,

697   long-range transport and local sources. Since these layers are confined mostly to the lower troposphere, the temperatures are

698   in the range of 27 to below 0^0C. From the above statistics (pre-monsoon and monsoon cases) it may be stated that the

699   mean/median value of CI for the non-spherical particle layer is distributed between 11 and 15, irrespective of environmental

700   humidity and season. BSR values for the non-spherical layer are between 1.4 and 3.5 at 455 nm, whereas little spread in the

701   red channel.

702   **3.4. Illustration of the aerosol-cloud relationship**

703   In this section, an attempt is made to demonstrate the method to identify the relationship, if any, between aerosol

704   and cloud properties observed using balloon observations of the BACIS campaigns. In the present analysis, we have

705   restricted ourselves to only liquid or low-level clouds as aerosol interactions in these cloud categories are well established

706   (Bruce A. Albrecht, 1989; Twomey, 1977).

707   The scheme (discussed in sec. 2) is applied to the 15 balloon soundings of the BACIS campaigns and 6 launches

708 have been observed with low-level cloud and aerosol layers. Further, a scatter plot between logarithm values of the median

709 cloud particle count of the cloud layer and logarithm of median values of aerosol (blue) backscatter below cloud base (for

710 300, 400 and 500m) is plotted in Fig. 13. A linear fit (line) of log-log values is also shown separately for all depths. It is

711 noticed for depths 100 and 200m below the cloud base relationship between aerosol, and the cloud cannot be discussed due

712 to a lack of data points of aerosol backscatter ratio from individual campaigns. This could be the result of the elimination of

713 the high value of COBALD particle backscatter (>3.15) observed in this region (100 and 200m below cloud base). In the

714 cloud boundaries of about 100 and 200m below the cloud base, an intermediate region exists where aerosol transformation to

715 cloud particle/growth takes place. Hence it is tricky to have the aerosol observation in this region. On the other hand, with

716 similar elimination criteria (Section 2), aerosol backscatter could be obtained (from all 5 campaigns) for depths 300m

717 onwards (up to 500m) from the cloud base. A good positive relationship is found between aerosol backscatter and cloud

718 particle count with a statistically significant Pearson correlation coefficient of about 0.9 and slope (ACI index) of 0.77 and

719 0.86 when the aerosol is considered from 300 and 400m below the cloud base, respectively. For a depth of 500m from the

720 cloud base, the slope has decreased to 0.67 (correlation coefficient is also not significant with p-value >0.05) indicating

721 aerosol influence weakens if the region below 400m from the cloud base is considered. Therefore, it may be better to

722 consider aerosols up to a depth of 400m (below the cloud base) for understanding their influence on cloud properties. It is

723 also emphasized that the slope (ACI index) value obtained in this analysis at all depths is well within the theoretical range of

724 0 to 1. However, with a greater number of balloon soundings, it might be possible to have statistically significant aerosol

725 data after constraining similar background/meteorological conditions to delineate their possible effects. Data obtained on 04

726 February 2020 was not considered in the analysis due to the high values of COBALD. The individual uncertainties in BSRb

727 and Nc were assumed to be 5% and the combined uncertainty in the ACI index is estimated as discussed in Sec. 2.4.7

728 (equation.7). It is found that the combined uncertainty in the estimated ACI index is found from 0.01 to 0.23 and 0.08 to

729 0.13, respectively for particle backscatter data from 300 and 400m below cloud base.

730 **4. Summary**

731   The BACIS (Balloon-borne Aerosol Cloud Interaction Studies) field campaigns have been conceptualized and

732   successfully conducted using multiple instruments from Gadanki (13.45^0 N; 79.2^0 E), a location in Southern peninsular India.

733   Meteorological balloon payloads with a combination of lightweight and specialized sondes such as COBALD and CPS have

734   been launched for the first time before a CALIPSO satellite overpass (close by Gadanki). Ground-based Lidars

735   (MPL/Ceilometer/Mie lidar), and Radars (MST Radar/LAWP) were also operated during the campaign period. So far 15

736   balloon soundings have been conducted as part of the BACIS campaigns.

737   During the first two (pilot) campaigns, all essential ground-based and space-borne instruments were made available.

738   Balloon-borne in-situ measurements (CPS and COBALD) are assessed using the data from ground/spaceborne remote

739   sensing instruments (CALIPSO, MPL and a Mie lidar) from two pilot campaigns (early hours of 6 June and 8 July 2017).

740   The comparison shows reasonable agreement within in-situ measurements as well as between ground-based/space-borne and

741   in-situ measurements. It is observed that the in-situ balloon soundings using a combination of specialized (COBALD and

742   CPS) sondes adds to the cloud and aerosol information than can be obtained from an individual ground/spaceborne

743   instrument.

744   To discriminate aerosol from clouds in a profile, combined observations of COBALD and CPS from a campaign

745   held on 27 June 2019 were inferred in detail. Using CPS data, liquid supercooled, and ice clouds were identified. COBALD

746   data of BSR corresponding to the ice clouds was found to be 1-10 (at blue channel) and CI of 10 to 20. In addition to cloud

747   features, CPS has also detected cloud particle layers at low altitudes (under dry conditions). These layers may be regarded as

748   non-spherical (coarse mode) aerosol particle layers as ice clouds (with non-spherical cloud particles) cannot exist at lower

749   heights. An attempt is also made to infer the size of cloud particles using the CPS data of intensity of scattered light (I55)

750   and the COBALD colour index. Based on CPS scattered light, the liquid droplet size (for the above case) is estimated to be

751   2-14 µm, and for ice particles, it is a combination of particles with 80-140 µm and 2-14 µm. The estimates of ice particle

752   sizes using CI data from COBALD supported the size interpretations of ice particles by CPS.

753   Further, combined observations from COBALD and CPS (BSR, CI, and peak particle number concentration data

754   based on information on the cloud phase) are analyzed from multiple (eight) balloon soundings from BACIS Campaigns.

755   From these statistics, it is found that the mean value of CI of ice cloud is found between 18 and 20. BSR (at both

756 wavelengths) have a wide range of values hence threshold values for ice clouds could not be arrived at. However, in some

757 cases, BSR increased with ice clouds of more droplet number concentration. In the case of non-spherical particle (aerosol)

758 layers (in the lower troposphere), the mean values of CI and BSR (at 455 nm) are found to be between 11 to 15 and 1.4 to

759 3.5, respectively. These non-spherical particle layers may correspond to coarse mode (dust) aerosols as discussed.

760   The relationship between aerosol and cloud in low-level (liquid) clouds is illustrated using balloon data from

761 BACIS campaigns. CPS cloud particle count and COBALD particle backscatter at the blue channel were considered as cloud

762 and aerosol proxies, respectively. A scheme is developed to carefully identify the cloud layers from CPS data and particle

763 (aerosol) backscatter below the cloud from COBALD data (in a profile). However, the relationships were analyzed

764 separately using particle backscatter data from 100 to 500m below the base height for the first cloud layer. The results show

765 a statistically significant correlation of 0.9 and a slope (Aerosol-Cloud Interaction index, ACI) of 0.7 (0.86) obtained

766 between particle backscatter from 300m (500m) below the cloud base and the corresponding cloud particle count. The ACI

767 index value obtained is well within the theoretical limits of 0 to 1 indicative of the aerosol activation process of the cloud.

768 The uncertainty in the estimated value of the ACI index is 0.01 to 0.23 and 0.08 to 0.13, respectively for backscatter data

769 from 300 and 400m below the cloud base.

770   Statistical estimates/threshold value of CI, BSR for cloud (liquid/super-cooled/ice) and non-spherical particles

771 attempted here will greatly help to separate a COBALD profile for aerosol and cloud. However, immediate efforts are

772 needed to understand the portion of the COBALD profile with no cloud detection from CPS. This portion of the COBALD

773 profile may correspond to either aerosol with fine mode particles and/or a thin cloud not detectable by a CPS. On the other

774 hand, estimates of size discussed here (from CPS, COBALD) are purely based on Mie theory and laboratory data. However,

775 with assumptions of the log-normal distribution of particles and measurements from COBALD (BSR, CI), the theoretical

776 estimate of the particle size distribution of aerosol/cloud is possible. It makes sense to cross-check rough estimates of size

777 from a CPS with COBALD size distributions rather than using CI variations. It is also planned to add a size distribution

778 measurement to the balloon payload for cross-verification and validation. Apart from this, in some of the cases, we have

779 noticed COBALD return signal saturated for liquid/supercooled cloud in the presence of a thick liquid cloud. Hence the

780 information from a greater number of future launches will help to conclude the statistical figures/threshold values for liquid

781 clouds as well as other cases of clouds, to discriminate the aerosol/cloud in a profile and to better quantify the aerosol-cloud

782 relationship. Further to this, attempts will be made to quantify aerosol-cloud interactions (with the multi-instrument data),

783 particularly the role of vertical wind and turbulence on the aerosol-cloud interactions, and ice cloud interactions, among

784 others. In a nutshell, the results presented in the study indeed demonstrate the potential of the observational

785 approach/method, to understand the aerosol-cloud process.

786 **Code/Data Availability**

787   Campaign data generated in the study is made available to the public on Zenodo (10.5281/zenodo.5749293). Data

788 will also be shared with the interested users under the collaboration.

789 **Author Contribution**

790   RKV is responsible for Conceptualization, Conducting experiments, Formal analysis, Visualization, Investigation,

791 Writing-original draft preparation; VRM is responsible for Supervision, helping in Visualization, Writing-review and

792 editing. FM, HR and FGW are responsible for Writing-review and editing; MBL, RRM, and RN helped in Visualization,

793 Writing-review and editing; RN, ARST, HKA, and RBS helped in conducting the experiment, Writing-review and editing;

794 **Competing interest**

795   The authors declare that they have no conflict of interest.

796 **Acknowledgements**

797 The authors would like to thank the Director, NARL for supporting of conducting the field campaigns from NARL, Gadanki.

798 Special thanks to the RADG and ASDG group members of NARL for their cooperation in the operation of Indian MST

799 Radar, LAWP and Mie Lidar, respectively, during the launch period. We also would like to express our thanks to the staff

800 members of ARTG, the balloon launch facility of NARL for extending their kind support for smoothly conducting balloon

801 launches and recovery. The CALIPSO science team is credited for providing the CALIOP data analysed in the study freely

802 available on their webpage (https://www.calipso.larc.nasa.gov). MOSDAC website (https://www.mosdac.gov.in/gallery-

803 products) is credited for providing images of brightness temperature used in the discussion. We are also thankful to the

804 Hysplit team for facilitating the running of the HYSPLIT model on their server to simulate the air parcel back trajectories as

805 per the requirement. Screen shot of the observational site is taken from the Google maps. We are thankful to Dr Simone

806 Lollie for kindly agreeing to serve as editor of the manuscript and also thankful to the two anonymous reviewers for their

807 constructive comments and suggestions.

808 **References**

809 Abbott, T. H. and Cronin, T. W.: Through Increases in Humidity, Science (80-.)., 85(January), 83–85, 2021.

810 Brabec, M., Wienhold, F. G., Wüest, M., Krieger, U. and Peter, T.: A novel radiosonde payload to study upper tropospheric /

811 lower stratospheric aerosol and clouds, 2008.

812 Brabec, M., Wienhold, F. G., Luo, B. P., VÃmel, H., Immler, F., Steiner, P., Hausammann, E., Weers, U. and Peter, T.:

813 Particle backscatter and relative humidity measured across cirrus clouds and comparison with microphysical cirrus

814 modelling, Atmos. Chem. Phys., 12(19), 9135–9148, doi:10.5194/acp-12-9135-2012, 2012.

815 BRUCE A. ALBRECHT: Aerosols, Cloud Microphysics, and Fractional Cloudiness, Science (80-.)., 245(4247), 24–29,

816 1989.

817 Brunamonti, S., Jorge, T., Oelsner, P., Hanumanthu, S., Singh, B. B., Ravi Kumar, K., Sonbawne, S., Meier, S., Singh, D.,

818 Wienhold, F. G., Ping Luo, B., Boettcher, M., Poltera, Y., Jauhiainen, H., Kayastha, R., Karmacharya, J., DIrksen, R., Naja,

819 M., Rex, M., Fadnavis, S. and Peter, T.: Balloon-borne measurements of temperature, water vapor, ozone and aerosol

820 backscatter on the southern slopes of the Himalayas during StratoClim 2016-2017, Atmos. Chem. Phys., 18(21), 15937–

821 15957, doi:10.5194/acp-18-15937-2018, 2018.

822 Brunamonti, S., Martucci, G., Romanens, G., Poltera, Y., Wienhold, F., Haefele, A. and Navas-Guzmán, F.: Validation of

823 aerosol backscatter profiles from Raman lidar and ceilometer using balloon-borne measurements, Atmos. Chem. Phys.

824 Discuss., (May), 1–31, doi:10.5194/acp-2020-294, 2020.

825 Cherian, T., Kumar, Y. B., Reddy, B. S., Optics, G., Limited, A., Nr, R. S. and Road, N.: LIDAR for Atmospheric

826 Measurement and Probing, , 5(84), 5114–5124, 2014.

827 Cirisan, A., Luo, B. P., Engel, I., Wienhold, F. G., Sprenger, M., Krieger, U. K., Weers, U., Romanens, G., Levrat, G.,

828 Jeannet, P., Ruffieux, D., Philipona, R., Calpini, B., Spichtinger, P. and Peter, T.: Balloon-borne match measurements of

829 midlatitude cirrus clouds, Atmos. Chem. Phys., 14(14), 7341–7365, doi:10.5194/acp-14-7341-2014, 2014.

830 COAKLEY, J. A., BERNSTEIN, R. L. and DURKEE, P. A.: Effect of Ship-Stack Effluents on Cloud Reflectivity, Science

831 (80-.)., 237(4818), 1020 LP – 1022, doi:10.1126/science.237.4818.1020, 1987.

832 Corrigan, C. E., Roberts, G. C., Ramana, M. V., Kim, D. and Ramanathan, V.: Capturing vertical profiles of aerosols and

833 black carbon over the Indian Ocean using autonomous unmanned aerial vehicles, Atmos. Chem. Phys., 8(3), 737–747,

834 doi:10.5194/acp-8-737-2008, 2008.

835 Costantino, L. and Bréon, F. M.: Analysis of aerosol-cloud interaction from multi-sensor satellite observations, Geophys.

836 Res. Lett., 37(11), 1–5, doi:10.1029/2009GL041828, 2010.

837 Deshler, T., Hervig, M. E., Hofmann, D. J., Rosen, J. M. and Liley, J. B.: Thirty years of in situ stratospheric aerosol size

838 distribution measurements from Laramie, Wyoming (41°N), using balloon-borne instruments, J. Geophys. Res. Atmos.,

839 108(5), 1–13, doi:10.1029/2002jd002514, 2003.

840 Fan, J., Wang, Y., Rosenfeld, D. and Liu, X.: Review of aerosol-cloud interactions: Mechanisms, significance, and

841 challenges, J. Atmos. Sci., 73(11), 4221–4252, doi:10.1175/JAS-D-16-0037.1, 2016.

842 Fan, J., Rosenfeld, D., Zhang, Y., Giangrande, S. E., Li, Z., Machado, L. A. T., Martin, S. T., Yang, Y., Wang, J., Artaxo, P.,

843 Barbosa, H. M. J., Braga, R. C., Comstock, J. M., Feng, Z., Gao, W., Gomes, H. B., Mei, F., Pöhlker, C., Pöhlker, M. L.,

844 Pöschl, U. and de Souza, R. A. F.: Substantial convection and precipitation enhancements by ultrafine aerosol particles,

845 Science (80-.)., 359(6374), 411–418, doi:10.1126/science.aan8461, 2018.

846 Feingold, G., Eberhard, W. L., Veron, D. E. and Previdi, M.: First measurements of the Twomey indirect effect using

847 ground-based remote sensors, Geophys. Res. Lett., 30(6), 19–22, doi:10.1029/2002GL016633, 2003.

848 Feingold, G., Furrer, R., Pilewskie, P., Remer, L. A., Min, Q. and Jonsson, H.: Aerosol indirect effect studies at Southern

849 Great Plains during the May 2003 Intensive Operations Period, J. Geophys. Res. Atmos., 111(5), 1–13,

850 doi:10.1029/2004JD005648, 2006.

851 Fujiwara, M., Shiotani, M., Hasebe, F., Vömel, H., Oltmans, S. J., Ruppert, P. W., Horinouchi, T. and Tsuda, T.:

852 Performance of the Meteolabor "Snow White" chilled-mirror hygrometer in the tropical troposphere: Comparisons with the

853 Vaisala RS80 A/H-Humicap sensors, J. Atmos. Ocean. Technol., 20(11), 1534–1542, doi:10.1175/1520-

854 0426(2003)020<1534:POTMSW>2.0.CO;2, 2003.

855 Fujiwara, M., Sugidachi, T., Arai, T., Shimizu, K., Hayashi, M., Noma, Y., Kawagita, H., Sagara, K., Nakagawa, T.,

856 Okumura, S., Inai, Y., Shibata, T., Iwasaki, S. and Shimizu, A.: Development of a cloud particle sensor for radiosonde

857 sounding, Atmos. Meas. Tech., 9(12), 5911–5931, doi:10.5194/amt-9-5911-2016, 2016.

858 Girdwood, J., Smith, H., Stanley, W., Ulanowski, Z., Stopford, C., Chemel, C., Doulgeris, K. M., Brus, D., Campbell, D. and

859 MacKenzie, R.: Design and field campaign validation of a multi-rotor unmanned aerial vehicle and optical particle counter,

860 Atmos. Meas. Tech., 13(12), 6613–6630, doi:10.5194/amt-13-6613-2020, 2020.

861 Girdwood, J., Stanley, W., Stopford, C. and Brus, D.: Simulation and Field Campaign Evaluation of an Optical Particle

862 Counter on a Fixed-Wing UAV, Atmos. Meas. Tech. Discuss., (October), 1–26, 2021.

863 Grosvenor, D. P., Sourdeval, O., Zuidema, P., Ackerman, A., Alexandrov, M. D., Bennartz, R., Boers, R., Cairns, B., Chiu,

864 J. C., Christensen, M., Deneke, H., Diamond, M., Feingold, G., Fridlind, A., Hünerbein, A., Knist, C., Kollias, P., Marshak,

865 A., McCoy, D., Merk, D., Painemal, D., Rausch, J., Rosenfeld, D., Russchenberg, H., Seifert, P., Sinclair, K., Stier, P.,

866 van Diedenhoven, B., Wendisch, M., Werner, F., Wood, R., Zhang, Z. and Quaas, J.: Remote Sensing of Droplet Number

867 Concentration in Warm Clouds: A Review of the Current State of Knowledge and Perspectives, Rev. Geophys., 56(2), 409–

868 453, doi:10.1029/2017RG000593, 2018.

869 Gupta, G., Ratnam, M. V., Madhavan, B. L., Prasad, P. and Narayanamurthy, C. S.: Vertical and spatial distribution of

870 elevated aerosol layers obtained using long-term ground-based and space-borne lidar observations, Atmos. Environ.,

871 246(December 2020), 118172, doi:10.1016/j.atmosenv.2020.118172, 2021.

872 Hanumanthu, S., Vogel, B., Müller, R., Brunamonti, S., Fadnavis, S., Li, D., Ölsner, P., Naja, M., Singh, B. B., Kumar, K.

873 R., Sonbawne, S., Jauhiainen, H., Vömel, H., Luo, B., Jorge, T., Wienhold, F. G., Dirkson, R. and Peter, T.: Strong day-to-

874 day variability of the Asian Tropopause Aerosol Layer (ATAL) in August 2016 at the Himalayan foothills, Atmos. Chem.

875 Phys., 20(22), 14273–14302, doi:10.5194/acp-20-14273-2020, 2020.

876 Haywood, J. and Boucher, O.: Estimates of the direct and indirect radiative forcing due to tropospheric aerosols: A review,

Rev. Geophys., 38(4), 513–543, doi:10.1029/1999RG000078, 2000.

Inoue, J., Sato, K., Tobo, Y., Taketani, F. and Maturilli, M.: Advanced method for estimating the number concentration of cloud water and liquid water content observed by cloud particle sensor sondes, Atmos. Meas. Tech. Discuss., 1–35, doi:10.5194/amt-2020-476, 2021.

IPCC: Climate Change 2021: The Physical Science Basis. Contribution of Working Group I to the Sixth Assessment Report of the Intergovernmental Panel on Climate Change, edited by V. Masson-Delmotte, P. Zhai, A. Pirani, S. L. Connors, C. Péan, S. Berger, N. Caud, Y. Chen, L. Goldfarb, M. I. Gomis, M. Huang, K. Leitzell, E. Lonnoy, J. B. R. Matthews, T. K. Maycock, T. Waterfield, O. Yelekçi, R. Yu, and B. Zhou, Cambridge University Press, Cambridge, United Kingdom and New York, NY, USA., 2021.

Jain, C. D., Madhavan, B. L. and Ratnam, M. V.: Source apportionment of rainwater chemical composition to investigate the transport of lower atmospheric pollutants to the UTLS region, Environ. Pollut., 248, 166–174, doi:10.1016/j.envpol.2019.02.007, 2019.

Jose, S., Nair, V. S. and Babu, S. S.: Anthropogenic emissions from South Asia reverses the aerosol indirect effect over the northern Indian Ocean, Sci. Rep., 10(1), 1–8, doi:10.1038/s41598-020-74897-x, 2020.

Kezoudi, M., Tesche, M., Smith, H., Tsekeri, A., Baars, H., Dollner, M., Estellés, V., Bühl, J., Weinzierl, B., Ulanowski, Z., Müller, D. and Amiridis, V.: Measurement report: Balloon-borne in situ profiling of Saharan dust over Cyprus with the UCASS optical particle counter, Atmos. Chem. Phys., 21(9), 6781–6797, doi:10.5194/acp-21-6781-2021, 2021.

Kobayashi, E., Hoshino, S., Iwabuchi, M., Sugidachi, T., Shimizu, K. and Fujiwara, M.: Comparison of the GRUAN data products for Meisei RS-11G and Vaisala RS92-SGP radiosondes at Tateno (36.06°N, 140.13°E), Japan, Atmos. Meas. Tech., 12(6), 3039–3065, doi:10.5194/amt-12-3039-2019, 2019.

Koren, I., Remer, L. A., Altaratz, O., Martins, J. V. and Davidi, A.: Aerosol-induced changes of convective cloud anvils produce strong climate warming, Atmos. Chem. Phys., 10(10), 5001–5010, doi:10.5194/acp-10-5001-2010, 2010.

Kulkarni, J. R., Maheskumar, R. S., Morwal, S. B., Padma Kumari, B., Konwar, M., Deshpande, C. G., Joshi, R. R., Bhalwankar, R. V., Pandithurai, G., Safai, P. D., Narkhedkar, S. G., Dani, K. K., Nath, A., Nair, S., Sapre, V. V., Puranik, P. V., Kandalgaonkar, S. S., Mujumdar, V. R., Khaladkar, R. M., Vijayakumar, R., Prabha, T. V. and Goswami, B. N.: The cloud aerosol interaction and precipitation enhancement experiment (CAIPEEX): Overview and preliminary results, Curr. Sci., 102(3), 413–425, 2012.

L'Ecuyer, T. S.: Touring the atmosphere aboard the A-Train (vol 63, pg 36, 2010), Phys. Today, 64(8), 10, 2011.

Lohmann, U.: Aerosol effects on clouds and climate, Space Sci. Rev., 125(1–4), 129–137, doi:10.1007/s11214-006-9051-8, 2006.

Lohmann, U. and Feichter, J.: Global indirect aerosol effects: a review, Atmos. Chem. Phys. Discuss., 4(6), 7561–7614, doi:10.5194/acpd-4-7561-2004, 2004.

Mamali, D., Marinou, E., Sciare, J., Pikridas, M., Kokkalis, P., Kottas, M., Binietoglou, I., Tsekeri, A., Keleshis, C.,

911   Engelmann, R., Baars, H., Ansmann, A., Amiridis, V., Russchenberg, H. and Biskos, G.: Vertical profiles of aerosol mass

912   concentration derived by unmanned airborne in situ and remote sensing instruments during dust events, Atmos. Meas. Tech.,

913   11(5), 2897–2910, doi:10.5194/amt-11-2897-2018, 2018.

914   McComiskey, A. and Feingold, G.: The scale problem in quantifying aerosol indirect effects, Atmos. Chem. Phys., 12(2),

915   1031–1049, doi:10.5194/acp-12-1031-2012, 2012.

916   McComiskey, A., Feingold, G., Frisch, A. S., Turner, D. D., Miller, M. A., Chiu, J. C., Min, Q. and Ogren, J. A.: An

917   assessment of aerosol-cloud interactions in marine stratus clouds based on surface remote sensing, J. Geophys. Res. Atmos.,

918   114(9), 1–15, doi:10.1029/2008JD011006, 2009.

919   Mishra, M. K., Rajeev, K., Thampi, B. V., Parameswaran, K. and Nair, A. K. M.: Micro pulse lidar observations of mineral

920   dust layer in the lower troposphere over the southwest coast of Peninsular India during the Asian summer monsoon season,

921   J. Atmos. Solar-Terrestrial Phys., 72(17), 1251–1259, doi:10.1016/j.jastp.2010.08.012, 2010.

922   Murphy, D. M. and Koop, T.: Review of the vapour pressures of ice and supercooled water for atmospheric applications, Q.

923   J. R. Meteorol. Soc., 131(608), 1539–1565, doi:10.1256/qj.04.94, 2005.

924   Narendra Reddy, N., Venkat Ratnam, M., Basha, G. and Ravikiran, V.: Cloud vertical structure over a tropical station

925   obtained using long-term high resolution Radiosonde measurements, Atmos. Chem. Phys. Discuss., 1–49, doi:10.5194/acp-

926   2018-194, 2018.

927   Pandit, A. K., Gadhavi, H., Ratnam, M. V., Jayaraman, A., Raghunath, K. and Rao, S. V. B.: Characteristics of cirrus clouds

928   and tropical tropopause layer: Seasonal variation and long-term trends, J. Atmos. Solar-Terrestrial Phys., 121(PB), 248–256,

929   doi:10.1016/j.jastp.2014.07.008, 2014.

930   Pandit, A. K., Gadhavi, H. S., Ratnam, M. V., Raghunath, K., Rao, S. V. B. and Jayaraman, A.: Long-term trend analysis

931   and climatology of tropical cirrus clouds using 16 years of lidar data set over Southern India, Atmos. Chem. Phys., 15(24),

932   13833–13848, doi:10.5194/acp-15-13833-2015, 2015.

933   Pandithurai, G., Takamura, T., Yamaguchi, J., Miyagi, K., Takano, T., Ishizaka, Y., Dipu, S. and Shimizu, A.: Aerosol effect

934   on cloud droplet size as monitored from surface-based remote sensing over East China Sea region, Geophys. Res. Lett.,

935   36(13), 1–5, doi:10.1029/2009GL038451, 2009.

936   Prasad, P., Raman, M. R., Ratnam, M. V., Ravikiran, V., Madhavan, B. L. and Bhaskara, S. V.: Nocturnal, seasonal and

937   intra-annual variability of tropospheric aerosols observed using ground-based and space-borne lidars over a tropical location

938   of India, Atmos. Environ., 213(May), 185–198, doi:10.1016/j.atmosenv.2019.06.008, 2019.

939   Radke, L. F., Coakley, J. A. and King, M. D.: Direct and remote sensing observations of the effects of ships on clouds,

940   Science (80-.)., 246(4934), 1146–1149, doi:10.1126/science.246.4934.1146, 1989.

941   Rao, P. B., Jain, A. R., Kishore, P., Balamuralidhar, P., Damle, S. H. and Viswanathan, G.: Indian MST radar 1. System

942   description and sample vector wind measurements in ST mode, Radio Sci., 30(4), 1125–1138, doi:10.1029/95RS00787,

943   1995.

944   Ratnam, M. V., Prasad, P., Raman, M. R., Ravikiran, V., Bhaskara, S. V., Murthy, B. V. K. and Jayaraman, A.: Role of

dynamics on the formation and maintenance of the elevated aerosol layer during monsoon season over south-east peninsular India, , 188(June), 43–49, doi:10.1016/j.atmosenv.2018.06.023, 2018.

Ravi Kiran Varaha, Venkat Ratnam Madineni, Masatomo Fujiwara, Herman Russchenberg, Frank G Weinhold, Madhavan B.L, Roja Raman M, Renju Nandan, Akhil Raj S T, Hemanth Kumar Alladiand Radindra Babu S: Balloon-borne Aerosol-Cloud Interaction Studies (BACIS): Field campaigns to understand and quantify aerosol effects on clouds, https://doi.org/10.5281/zenodo.5749293, 2021.

Redemann, J., Wood, R., Zuidema, P., Doherty, S., Luna, B., LeBlanc, S., Diamond, M., Shinozuka, Y., Chang, I., Ueyama, R., Pfister, L., Ryoo, J., Dobracki, A., da Silva, A., Longo, K., Kacenelenbogen, M., Flynn, C., Pistone, K., Knox, N., Piketh, S., Haywood, J., Formenti, P., Mallet, M., Stier, P., Ackerman, A., Bauer, S., Fridlind, A., Carmichael, G., Saide, P., Ferrada, G., Howell, S., Freitag, S., Cairns, B., Holben, B., Knobelspiesse, K., Tanelli, S., L'Ecuyer, T., Dzambo, A., Sy, O., McFarquhar, G., Poellot, M., Gupta, S., O'Brien, J., Nenes, A., Kacarab, M., Wong, J., Small-Griswold, J., Thornhill, K., Noone, D., Podolske, J., Schmidt, K. S., Pilewskie, P., Chen, H., Cochrane, S., Sedlacek, A., Lang, T., Stith, E., Segal-Rozenhaimer, M., Ferrare, R., Burton, S., Hostetler, C., Diner, D., Platnick, S., Myers, J., Meyer, K., Spangenberg, D., Maring, H. and Gao, L.: An overview of the ORACLES (ObseRvations of Aerosols above CLouds and their intEractionS) project: aerosol-cloud-radiation interactions in the Southeast Atlantic basin, Atmos. Chem. Phys., 1–82, doi:10.5194/acp-2020-449, 2020.

Rosen, J. M. and Kjome, N. T.: Backscattersonde: a new instrument for atmospheric aerosol research, Appl. Opt., 30(12), 1552, doi:10.1364/ao.30.001552, 1991.

Rosenfeld, D., Lohmann, U., Raga, G. B., O'Dowd, C. D., Kulmala, M., Fuzzi, S., Reissell, A. and Andreae, M. O.: Flood or drought: How do aerosols affect precipitation?, Science (80-.)., 321(5894), 1309–1313, doi:10.1126/science.1160606, 2008.

Rosenfeld, D., Sherwood, S., Wood, R. and Donner, L.: Climate Effects of Aerosol-Cloud Interactions, Science (80-.)., 343(6169), 379 LP – 380, doi:10.1126/science.1247490, 2014a.

Rosenfeld, D., Andreae, M. O., Asmi, A., Chin, M., Leeuw, G., Donovan, D. P., Kahn, R., Kinne, S., Kivekäs, N., Kulmala, M., Lau, W., Schmidt, K. S., Suni, T., Wagner, T., Wild, M. and Quaas, J.: Reviews of Geophysics, , 1–59, doi:10.1002/2013RG000441.Received, 2014b.

Sarna, K. and Russchenberg, H. W. J.: Ground-based remote sensing scheme for monitoring aerosol-cloud interactions, Atmos. Meas. Tech., 9(3), 1039–1050, doi:10.5194/amt-9-1039-2016, 2016.

Sarna, K. and Russchenberg, H. W. J.: Monitoring aerosol-cloud interactions at the CESAR Observatory in the Netherlands, Atmos. Meas. Tech., 10(5), 1987–1997, doi:10.5194/amt-10-1987-2017, 2017.

Sathiyamoorthy, V., Mahesh, C., Gopalan, K., Prakash, S., Shukla, B. P. and Mathur, A. K.: Characteristics of low clouds over the Arabian Sea, , 118(December), 489–503, doi:10.1002/2013JD020553, 2013.

Schmidt, J., Ansmann, A., Bühl, J., Baars, H., Wandinger, U., Müller, D. and Malinka, A. V.: Dual-FOV raman and Doppler lidar studies of aerosol-cloud interactions: Simultaneous profiling of aerosols, warm-cloud properties, and vertical wind, J. Geophys. Res., 119(9), 5512–5527, doi:10.1002/2013JD020424, 2014.

979   Schmidt, J., Ansmann, A., Bühl, J. and Wandinger, U.: Strong aerosol-cloud interaction in altocumulus during updraft
980   periods: Lidar observations over central Europe, Atmos. Chem. Phys., 15(18), 10687–10700, doi:10.5194/acp-15-10687-
981   2015, 2015.

982   Seinfeld, J. H., Bretherton, C., Carslaw, K. S., Coe, H., DeMott, P. J., Dunlea, E. J., Feingold, G., Ghan, S., Guenther, A. B.,
983   Kahn, R., Kraucunas, I., Kreidenweis, S. M., Molina, M. J., Nenes, A., Penner, J. E., Prather, K. A., Ramanathan, V.,
984   Ramaswamy, V., Rasch, P. J., Ravishankara, A. R., Rosenfeld, D., Stephens, G. and Wood, R.: Improving our fundamental
985   understanding of the role of aerosol-cloud interactions in the climate system, Proc. Natl. Acad. Sci. U. S. A., 113(21), 5781–
986   5790, doi:10.1073/pnas.1514043113, 2016.

987   Sena, E. T., McComiskey, A. and Feingold, G.: A long-term study of aerosol-cloud interactions and their radiative effect at
988   the Southern Great Plains using ground-based measurements, Atmos. Chem. Phys., 16(17), 11301–11318, doi:10.5194/acp-
989   16-11301-2016, 2016.

990   Small, J. D., Chuang, P. Y., Feingold, G. and Jiang, H.: Can aerosol decrease cloud lifetime?, Geophys. Res. Lett., 36(16),
991   1–5, doi:10.1029/2009GL038888, 2009.

992   Smith, H. R., Ulanowski, Z., Kaye, P. H., Hirst, E., Stanley, W., Kaye, R., Wieser, A., Stopford, C., Kezoudi, M., Girdwood,
993   J., Greenaway, R. and Mackenzie, R.: The Universal Cloud and Aerosol Sounding System (UCASS): A low-cost miniature
994   optical particle counter for use in dropsonde or balloon-borne sounding systems, Atmos. Meas. Tech., 12(12), 6579–6599,
995   doi:10.5194/amt-12-6579-2019, 2019.

996   Srinivasulu, P., Yasodha, P., Kamaraj, P., Rao, T. N., Jayaraman, A., Reddy, S. N. and Satyanarayana, S.: 1280-MHz active
997   array radar wind profiler for lower atmosphere: System description and data validation, J. Atmos. Ocean. Technol., 29(10),
998   1455–1470, doi:10.1175/JTECH-D-12-00030.1, 2012.

999   Stein, A. F., Draxler, R. R., Rolph, G. D., Stunder, B. J. B., Cohen, M. D. and Ngan, F.: Noaa's hysplit atmospheric transport
1000 and dispersion modeling system, Bull. Am. Meteorol. Soc., 96(12), 2059–2077, doi:10.1175/BAMS-D-14-00110.1, 2015.

1001 Twomey, S.: The Influence of Pollution on the Shortwave Albedo of Clouds, J. Atmos. Sci., 34(7), 1149–1152,
1002 doi:10.1175/1520-0469(1977)034<1149:TIOPOT>2.0.CO;2, 1977.

1003 Vernier, J., Fairlie, T. D., Natarajan, M., Wienhold, F. G., Bian, J., Martinsson, B. G., Crumeyrolle, S., Thomason, L. W. and
1004 Bedka, K. M.: Journal of Geophysical Research : Atmospheres, , doi:10.1002/2014JD022372.Received, 2015.

1005 Vernier, J. P., Fairlie, T. D., Deshler, T., Venkat Ratnam, M., Gadhavi, H., Kumar, B. S., Natarajan, M., Pandit, A. K., Akhil
1006 Raj, S. T., Hemanth Kumar, A., Jayaraman, A., Singh, A. K., Rastogi, N., Sinha, P. R., Kumar, S., Tiwari, S., Wegner, T.,
1007 Baker, N., Vignelles, D., Stenchikov, G., Shevchenko, I., Smith, J., Bedka, K., Kesarkar, A., Singh, V., Bhate, J., Ravikiran,
1008 V., Durga Rao, M., Ravindrababu, S., Patel, A., Vernier, H., Wienhold, F. G., Liu, H., Knepp, T. N., Thomason, L.,
1009 Crawford, J., Ziemba, L., Moore, J., Crumeyrolle, S., Williamson, M., Berthet, G., Jégou, F. and Renard, J. B.: BATAL: The
1010 balloon measurement campaigns of the Asian tropopause aerosol layer, Bull. Am. Meteorol. Soc., 99(5), 955–973,
1011 doi:10.1175/BAMS-D-17-0014.1, 2018.

1012 Vernier, J. P., Kalnajs, L., Diaz, J. A., Reese, T., Corrales, E., Alan, A., Vernier, H., Holland, L., Patel, A., Rastogi, N.,

1013   Wienhold, F., Carn, S., Krotkov, N. and Murray, J.: VolKilau: Volcano rapid response balloon campaign during the 2018

1014   Kilauea eruption, Bull. Am. Meteorol. Soc., 101(10), E1602–E1618, doi:10.1175/BAMS-D-19-0011.1, 2020.

1015   Weinzierl, B., Ansmann, A., Prospero, J. M., Althausen, D., Benker, N., Chouza, F., Dollner, M., Farrell, D., Fomba, W. K.,

1016   Freudenthaler, V., Gasteiger, J., Groß, S., Haarig, M., Heinold, B., Kandler, K., Kristensen, T. B., Mayol-Bracero, O. L.,

1017   Müller, T., Reitebuch, O., Sauer, D., Schäfler, A., Schepanski, K., Spanu, A., Tegen, I., Toledano, C. and Walser, A.: The

1018   Saharan aerosol long-range transport and aerosol-cloud-interaction experiment: Overview and selected highlights, Bull. Am.

1019   Meteorol. Soc., 98(7), 1427–1451, doi:10.1175/BAMS-D-15-00142.1, 2017.

1020   Wiegner, M., Madonna, F., Binietoglou, I., Forkel, R., Gasteiger, J., Geiß, A., Pappalardo, G., Schäfer, K. and Thomas, W.:

1021   What is the benefit of ceilometers for aerosol remote sensing? An answer from EARLINET, Atmos. Meas. Tech., 7(7),

1022   1979–1997, doi:10.5194/amt-7-1979-2014, 2014.

1023   Winker, D. M., Hunt, W. H. and McGill, M. J.: Initial performance assessment of CALIOP, Geophys. Res. Lett., 34(19), 1–

1024   5, doi:10.1029/2007GL030135, 2007.

1025

1026

 Tables

1028
1029 **Table 1.** List of instruments deployed (in BACIS) and the corresponding physical parameters obtained.
1030

Sl. No.	Instrument	Purpose	Physical quantity (Unit)
1	CALIPSO	Aerosol and cloud profiling	Total attenuated backscatter(km^{-1} sr^{-1})
2	MPL	Aerosol and cloud profiling	Backscatter coefficient($m^{-1}sr^{-1}$)
3	Mie Lidar	Aerosol and cloud profiling	Backscatter coefficient($km^{-1}sr^{-1}$)
4	COBALD	In-situ measurement of aerosol and cloud particles	Backscatter ratio
5	CPS	In situ measurement of cloud particles	Cloud particle number concentration(#/cc), degree of polarization(DOP)
6	MST Radar	3-D Wind components, turbulence	Horizontal and vertical wind components(m/s)
7	LAWP	3-D Wind components, turbulence	Horizontal and vertical wind components (m/s)
8	MWR	Meteorological parameters and cloud	Temperature(^{0}C), RH(%) and cloud liquid water content(g/m^3)
9	ICON	Ambient aerosol	BC concentration ($\mu g/m^3$), Scattering coefficient and absorption coefficient (m^{-1})
10	Ceilometer	Boundary layer, cloud and aerosol	Backscatter coefficient($km^{-1}sr^{-1}$)

1031
1032
1033
1034
1035
1036
1037
1038
1039
1040
1041
1042
1043
1044
1045
1046

1047   **Table. 2.** Date and time of the BACIS campaigns and the instruments operated during the corresponding campaigns.

1048

S. No.	Date & Time (LT)	MPL	Mie	Ceil	CPS	COB	MST	MWR	Aeth	CALI	LAWP
1	06-06-2017; 01:57	Y	Y	N	Y	Y	Y	N	Y	Y	Y
2	08-07-2017; 01:36	Y	Y	N	Y	Y	N	N	Y	Y	Y
3	29-09-2018; 01:46	Y	Y	N	Y	Y	N	N	Y	N	Y
4	01-11-2018; 22:13	N	Y	N	Y	Y	N	N	Y	N	Y
5	23-03-2019; 02:36	N	Y	Y	Y	Y	Y	N	Y	N	Y
6	30-04-2019; 23:16	N	Y	Y	Y	Y	Y	N	Y	N	Y
7	30-05-2019; 23:46	N	Y	Y	Y	Y	Y	N	Y	N	Y
8	27-06-2019; 23:45	N	Y	Y	Y	Y	Y	N	Y	N	Y
9	28-08-2019; 23:42	N	Y	Y	Y	Y	Y	N	Y	N	Y
10	09-10-2019; 23:36	N	Y	Y	Y	Y	Y	N	Y	N	Y
11	20-12-2019; 21:20	N	Y	Y	Y	Y	Y	Y	Y	N	Y
12	04-02-2020; 00:27	N	Y	Y	Y	Y	Y	N	Y	N	Y
13	10-03-2020; 00:26	N	Y	Y	Y	Y	Y	N	Y	N	Y
14	19-06-2020; 23:26	N	Y	Y	Y	Y	Y	Y	Y	N	Y
15	19-08-2020; 22:39	N	Y	Y	Y	Y	Y	N	Y	N	Y
MPL – Micro Pulse Lidar; Mie – Mie Lidar; Ceil – Ceilometer; CPS – Cloud Particle Sensor (CPS); COB – Compact Optical Backscatter AerosoL Detector (COBALD); MST – Indian MST Radar; LAWP – Lower Atmospheric Wind Profiler (LAWP); Aeth – Aethalometer; CALI – Calipso; MWR – Micro Wave Radiometer.											

1049

1050

1051 **Table 3.** Colour Index (CI) and other physical parameters of the ice clouds. The backscatter ratio (BSR) in normal (Italic)
1052 font is for a 450 nm (940 nm) channel.
1053

Date	Campaign no	Ice cloud altitude (km)	Temperature range (^{0}C)	RH condition	Mean (median) CI	Mean (median) BSR	Range of peak ice particle no conc. (#/cc)
06-Jun-2017	1	13- 15.5	-53 to -74	~ SRH	19.2 (19.2)	5.6(4.8) *90.4(73)*	10^{-2} to 10^{-1}
08-Jul-2017	2	10.5-16	-34 to -78	> SRH	18.7(18.6)	3(2.9) *37.5(35.2)*	10^{-2} to 10^{-1}
01-Nov-2018	4	12-12.6	-47 to -53	> SRH	19.5	17.2(17.5) *318(313.5)*	10^{-1} to 1
30-Apr-2019	6	9.3-16	-22 to -79	~SRH	19.4(19.3)	16.4(8.6) *302(147)*	10^{-1} to 1
30-May-2019	7	16.2-17.4	-78 to -84.5	<SRH	18	1.6(1.4) *12.2(8.7)*	10^{-3} to 10^{-2}
27-Jun-2019	8	9.4-10.7	-23.7 to -35.2	>SRH	19.3(17.9)	5.1(3.1) *74.8(43.2)*	10^{-1} to 1
19-Jun-2020	14	14.2-15.4	-62 to -75	<SRH	21	7.9(7.9) *147.4(143.2)*	10^{-1} to 1

1054
1055

1056

1057 **Table 4.** Colour Index (CI) and backscatter ratio (BSR) of non-spherical (coarse) particle layers as identified by a CPS
1058 sonde. The BSR in the normal (italic) font is 450 nm (940 nm). Bold (underlined) font values are observed in the monsoon
1059 (pre-monsoon) months.
1060

Campaign Date	Non-spherical layer altitude (km)	Temperature range (^{0}C)	RH range (%)	Mean (median) CI	Mean (median) BSR
06-Jun-2017	**0.5-2.5**	**27.6 to 15.5**	**63.5-81.3**	**12.3(12.5)**	**1.45(1.4)** *6.5(6)*
08-Jul-2017	**0.5-2.5**	**25.3 to 14.7**	**64.2-96.4**	**14.6(14.8)**	**2** *15.8*
29-Sep-2018	**0.5-1**	**22.6 to 20**	**92-94**	**12.3**	**3.3(3.2)** *30(29)*
27-Jun-2019	**0.5-1.5**	**27.6 to 19.8**	**57.3-70.3**	**11.4**	**1.6** *7.6*
19-Jun-2020	**0.5-2.5**	**28.8 to 14.2**	**57.2-94.4**	**12.6(12.8)**	**1.6** *8(8.1)*
23-Mar-2019	1.5-3.5	23 to 6.5	32.7-70.3	12.6(12.8)	2 *13*
30-Apr-2019	0.5-4	28 to 4.5	60.2-97.3	12.2(12.6)	3.3(2.6) *28(21.5)*
30-May-2019	0.5-5	28.8 to -0.1	60-98	11.7(11.6)	3.2(2.9) *25.7(22)*

1061
1062

1063
1064

1065
Figure 1. Schematic diagram showing the observational concept of the Balloon-borne Aerosol Cloud Interaction Studies (BACIS) campaign.
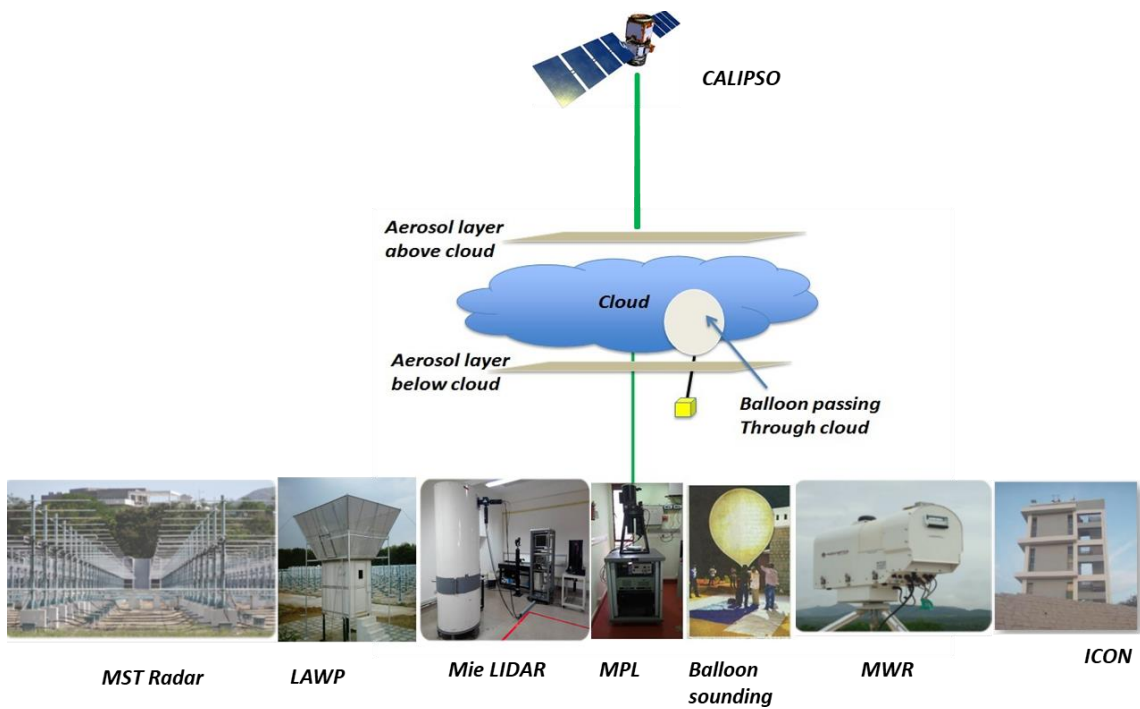
1068
1069
1070
1071
1072
1073
1074
1075
1076
1077
1078
1079
1080
1081
1082
1083
1084
1085
1086
1087
1088
1089
1090

1091
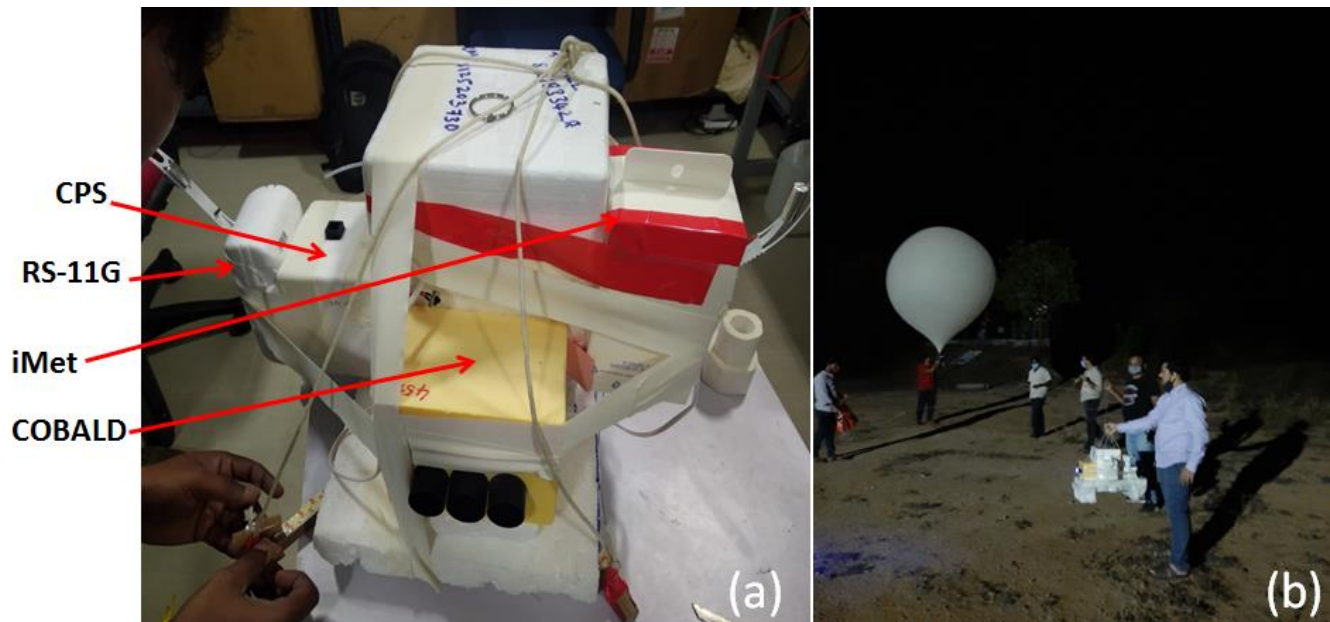
1092
1093
1094 **Figure 2.** Photograph shows (a) the balloon payload with COBALD, iMet radiosonde, CPS, RS-11G radiosonde, and (b)
1095 pre-launch preparations at the launch field with the payload and balloon.

1096

1097

1098

1099

1100

1101
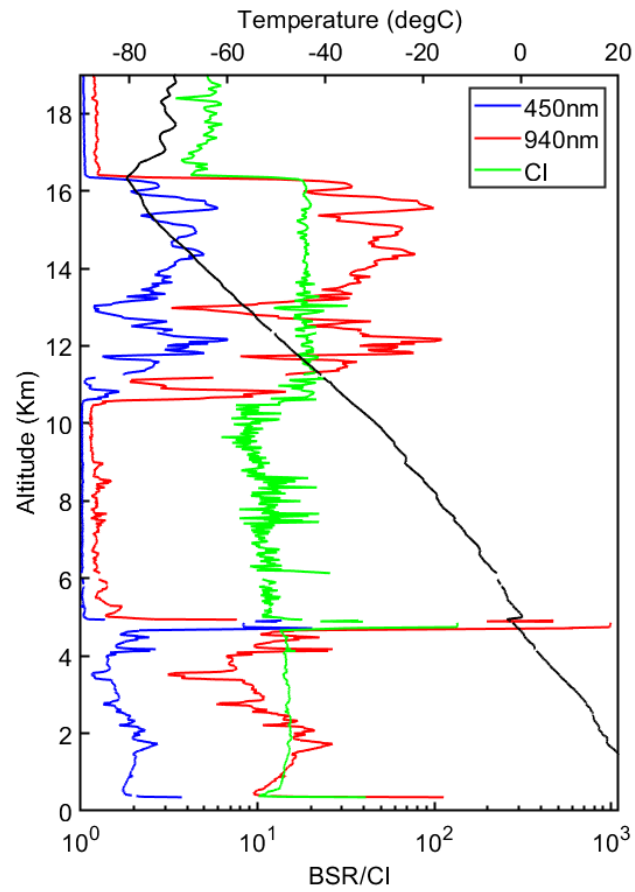
1102 **Figure 3**. Backscatter ratio (BSR) at blue (450 nm) and red (940 nm) channels were obtained using a COBALD sonde

1103   launched during the second pilot campaign (08 July 2017). Colour Index (CI) estimated from BSR at both channels is also

1104   shown (in green colour).

1105

1106

1107

1108

1109

1110

1111

1112

1113

1114

1115
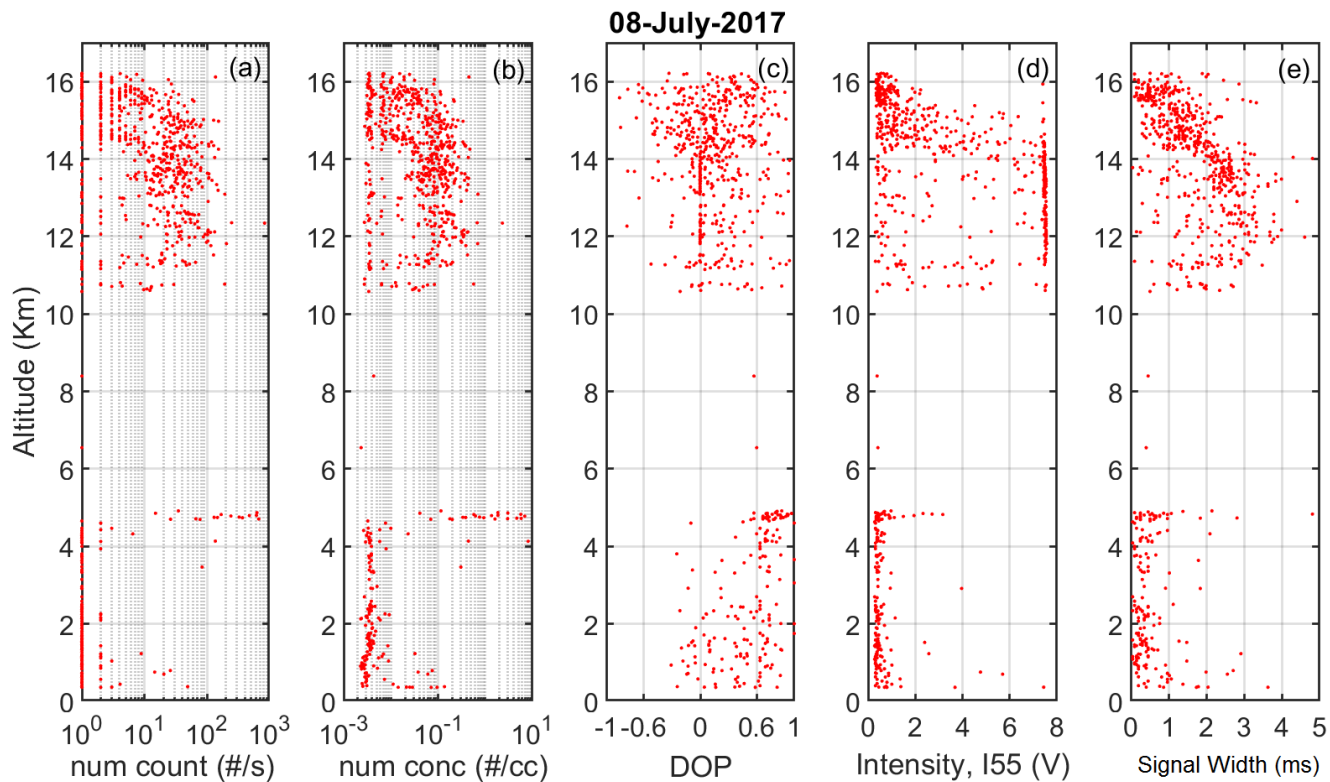
1116
1117
1118 **Figure 4.** CPS measurements collected from the second pilot campaign (08 July 2017) showing (a) cloud particle number
1119 count (corrected), #/s (b) cloud particle number concentration, #/cm^3 (c) Degree of polarization of a cloud particle, DOP
1120 (d) the intensity of light scattered at 55 degrees angle in Volts and (e) the particle signal width in ms.
1121
1122
1123
1124
1125
1126
1127
1128
1129
1130
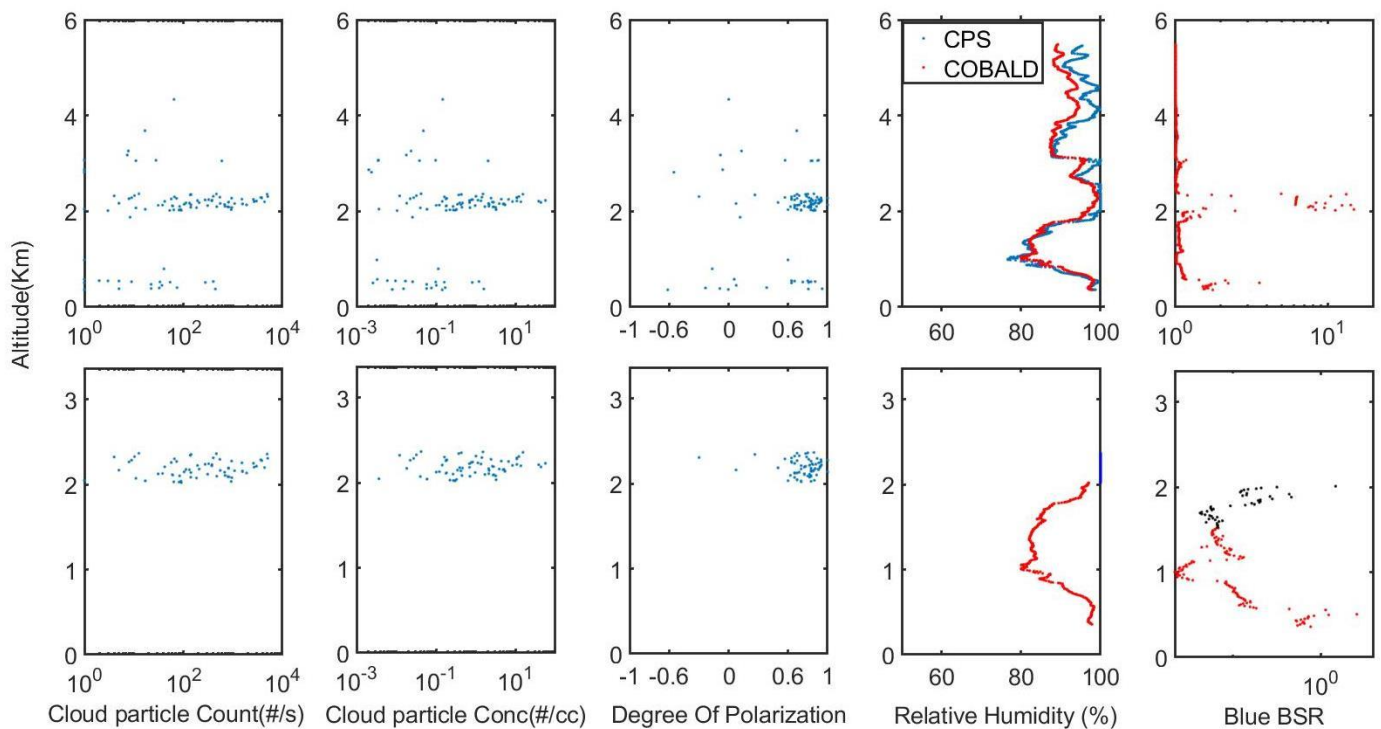
1131
1132
1133 **Figure 5**. The top panel shows COBALD and CPS observations from a sounding held on 01 November 2018 up to the
1134   altitude of 6 km (as the focus is on the liquid cloud region). The bottom panel shows the same parameters but for the
1135   portion of the same profile where liquid cloud (blue dots) and aerosol (from cloud base to 500 m below) were identified by
1136   the scheme.

1137
1138
1139
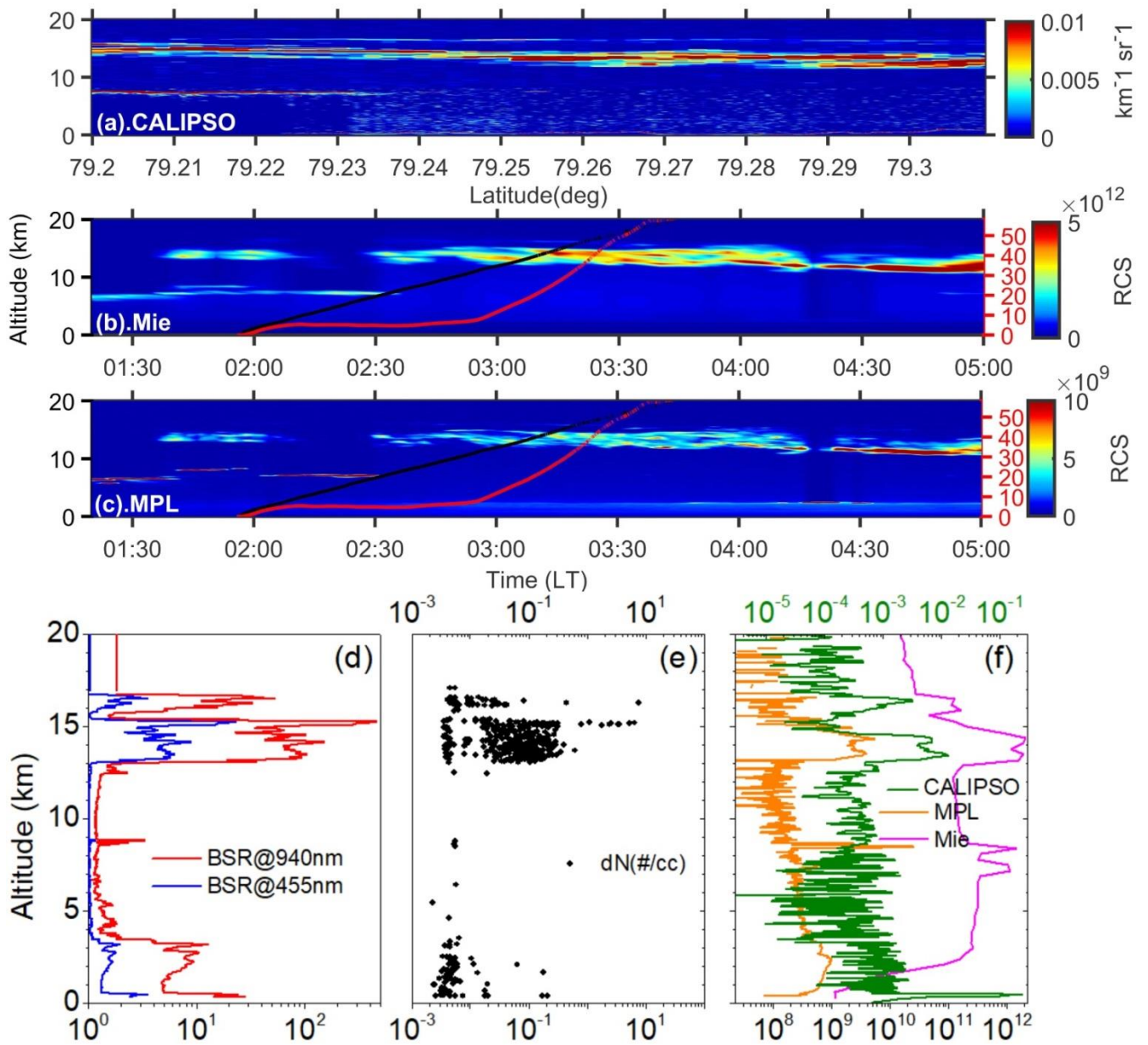
Figure 6. Multi-instrument data from a balloon sounding held in the early hours of 06 June 2017. The total attenuated backscatter from (a) CALIPSO and temporal variation in range corrected signal from (b) Mie lidar and (c) MPL. The red (black) lines overplotted on contour maps (b) and (c) represent balloon drift (altitude) in km with time. Drift as a function of time can be read with the right y-axis (red font) and altitude as a function of time can be read with the left y-axis. The profiles of BSR at two channels from COBALD (blue and red-coloured lines), particle number concentration from CPS (black coloured dots), RCS from MPL (orange), Mie lidar (magenta) and total attenuated backscatter from CALIPSO (olive green) lines shown in (d), (e) and (f) respectively.
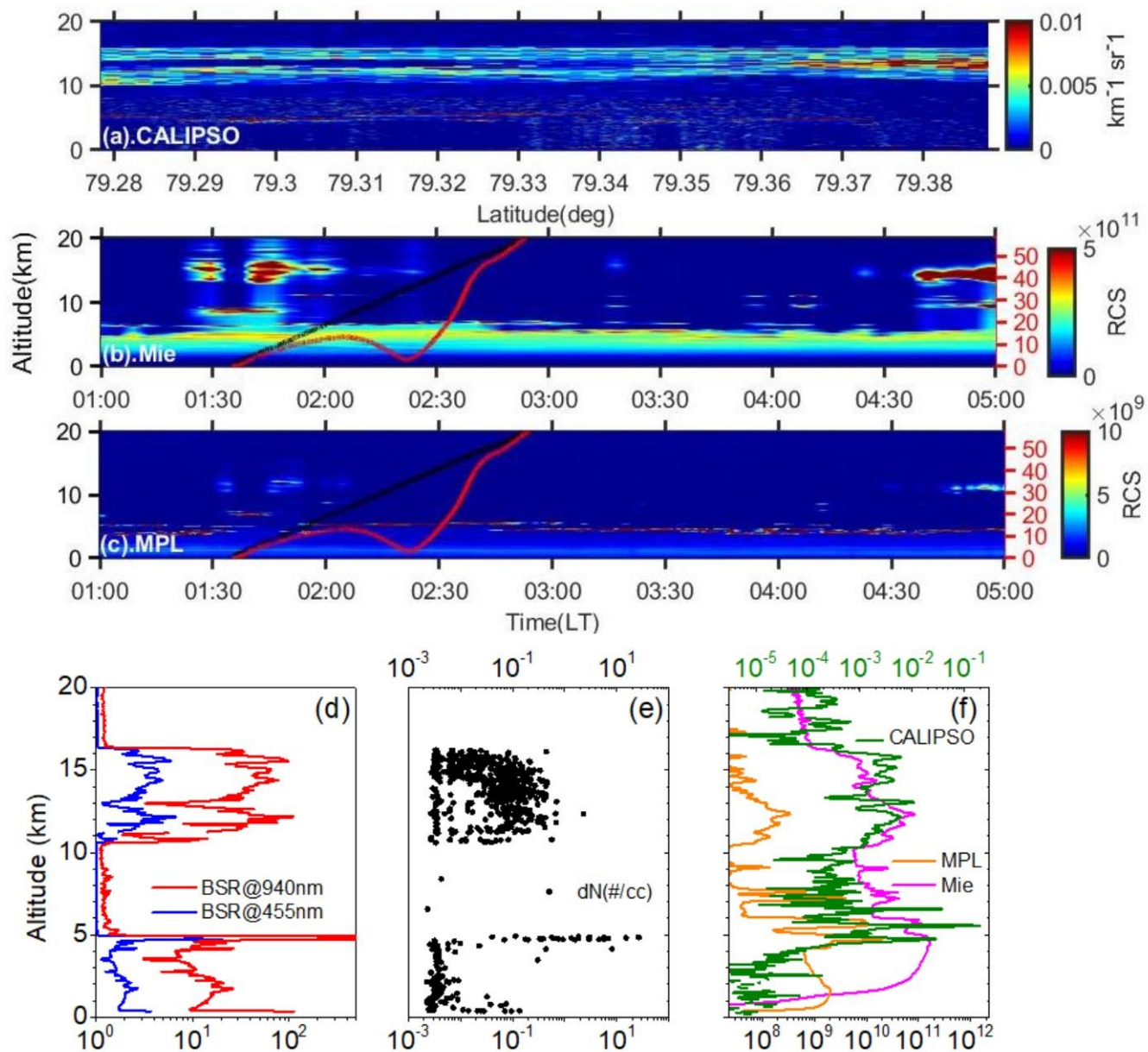
Figure 7. Same as Figure 6 but for the case of the second pilot campaign (08 July 2017).

1155
1156
1157 Figure.8: Google map of the balloon launch facility, remote sensing apparatus at NARL.

1158
1159
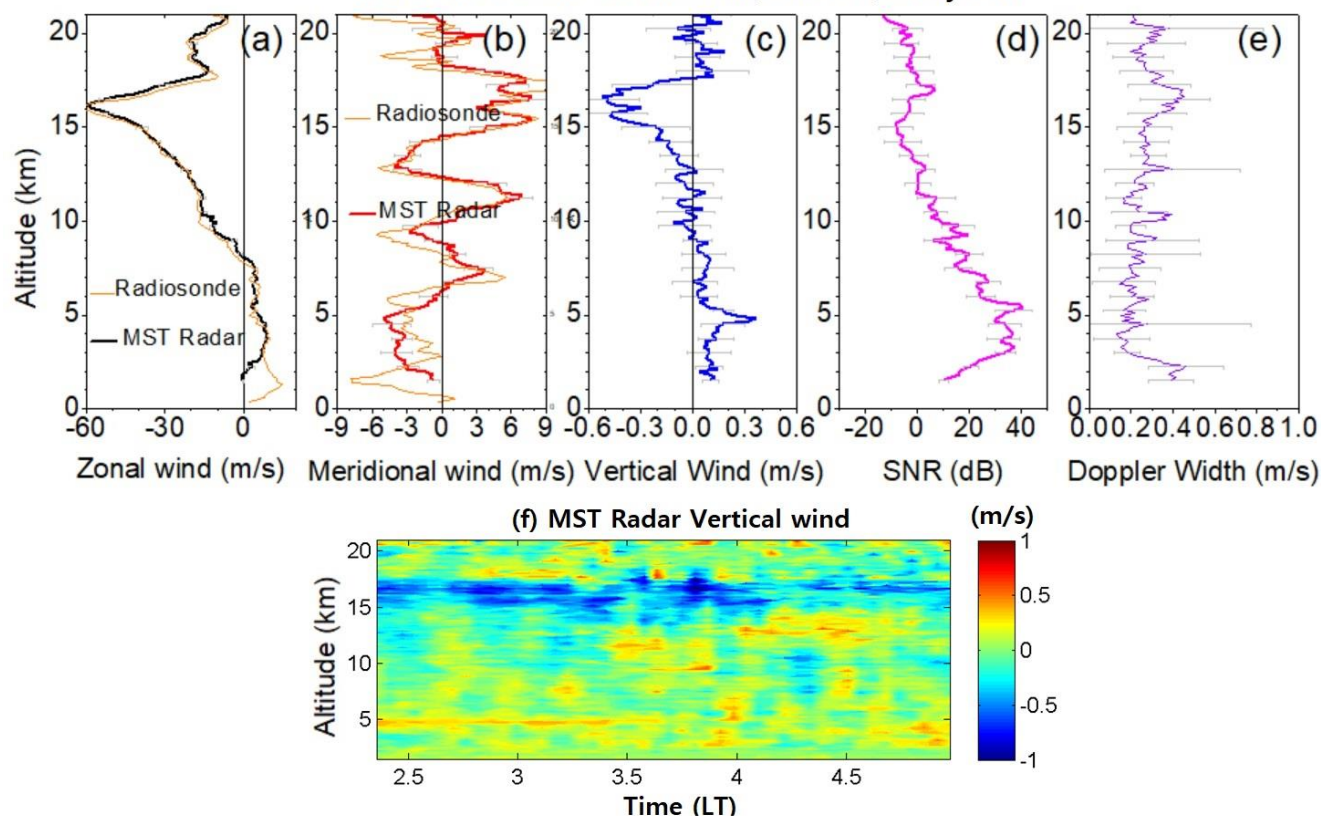
1160
1161
1162
1163 **Figure 9**. Profiles of (a) zonal wind, (b) meridional wind, (c) Vertical wind, (d) Signal to Noise Ratio (SNR) and (e) Doppler
1164   Width were obtained from Indian MST radar on 8 July 2017 averaged during 02:30 LT to 03:30 LT. Horizontal bars show
1165   standard deviation. Radiosonde observed zonal and meridional winds are also superimposed in the respective panels. (f)
1166   Time-altitude section of vertical wind obtained from Indian MST radar during the radiosonde launch time.
1167
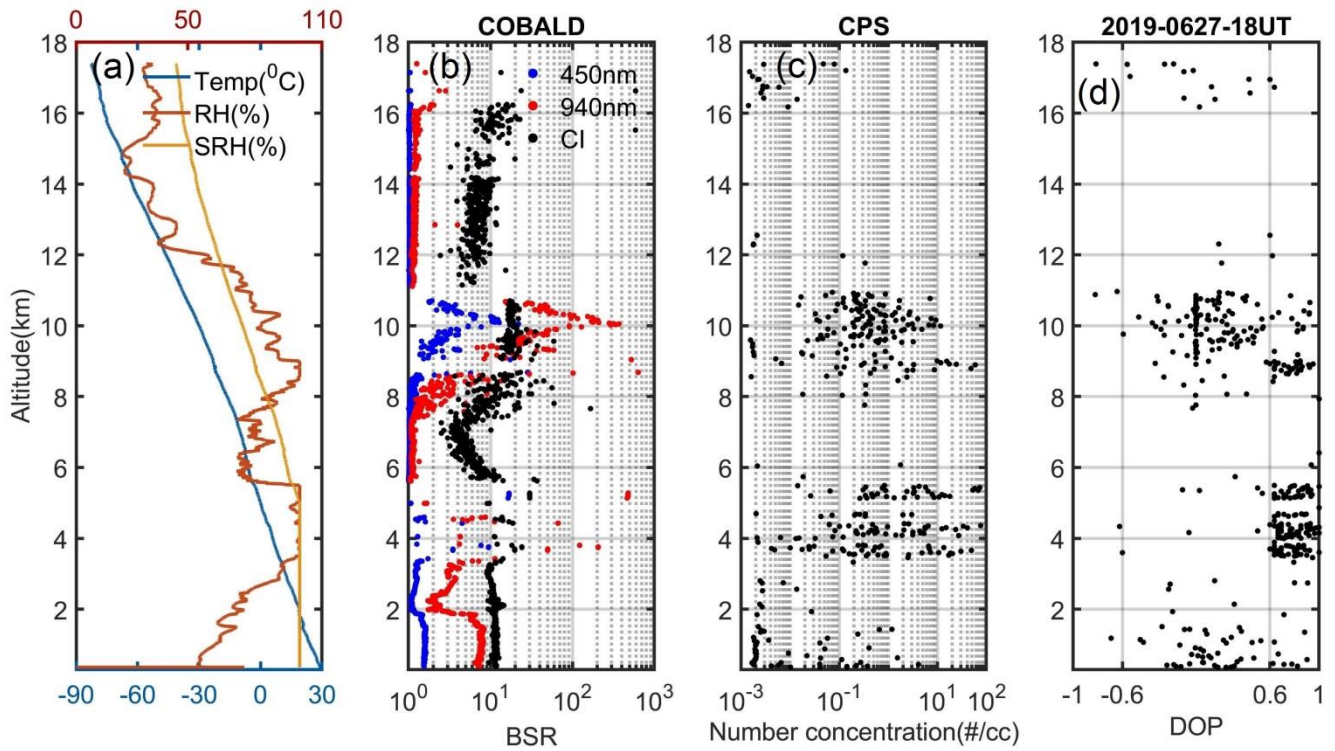
1168
1169   **Figure 10**. Combined observations of COBALD and CPS from balloon sounding were held on 27 June 2019 at 2330 LT. (a)
1170   Temperature (T), Relative humidity (RH) and Saturation Relative Humidity (SRH) (b) Backscatter ratio at 455 nm (blue),
1171   940 nm (red) and Colour Index (Black). (c) Cloud particle number concentration and (d) Degree of polarization (DOP).
1172
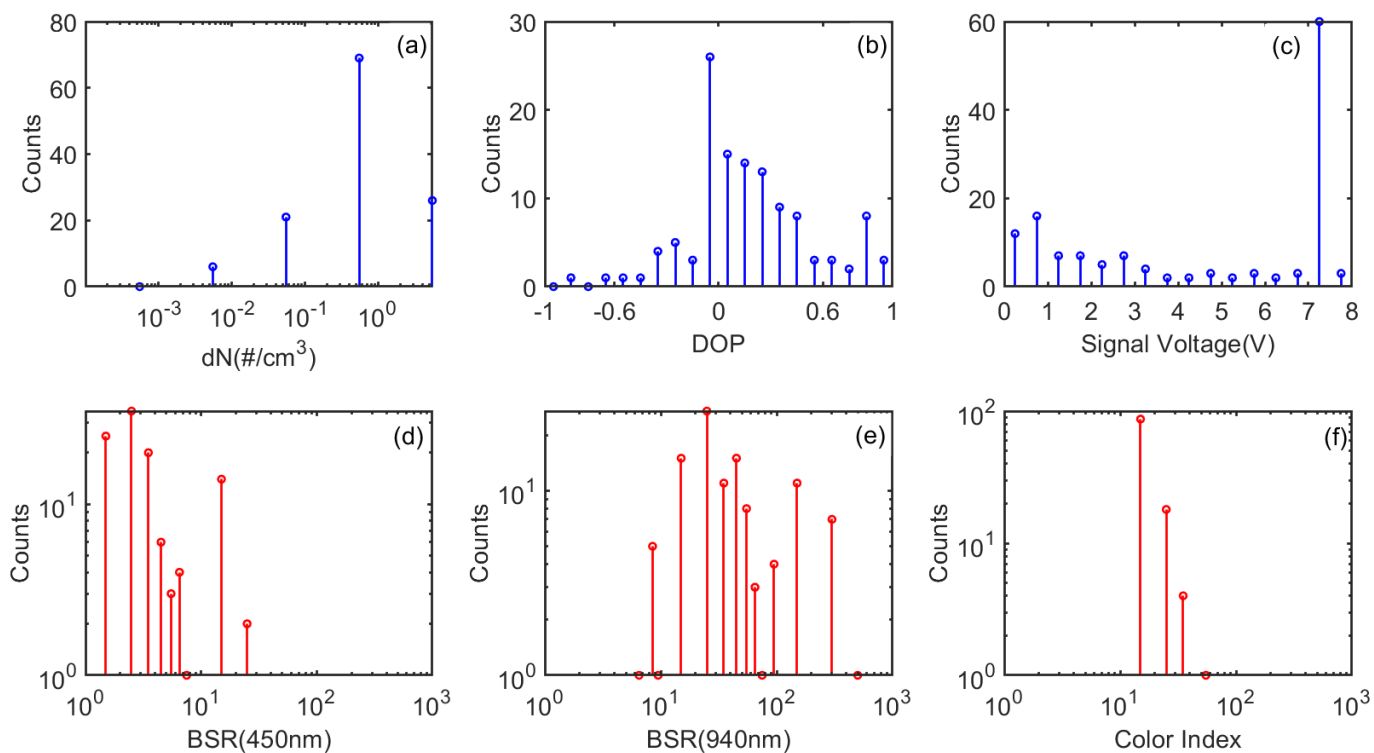
Figure 11. Histogram of (a) Droplet number concentration (dN) in #/cc (b) Degree of polarization (DOP) (c) Backscattered
signal (Volts) (d) Backscatter ratio at 455 nm, (e) Backscatter ratio at 940 nm and (f) Colour Index. The top panel shows
the data from CPS and the bottom panel from COBALD for the ice cloud layer between 9 and 11 km from the sounding
held on 27 June 2019.
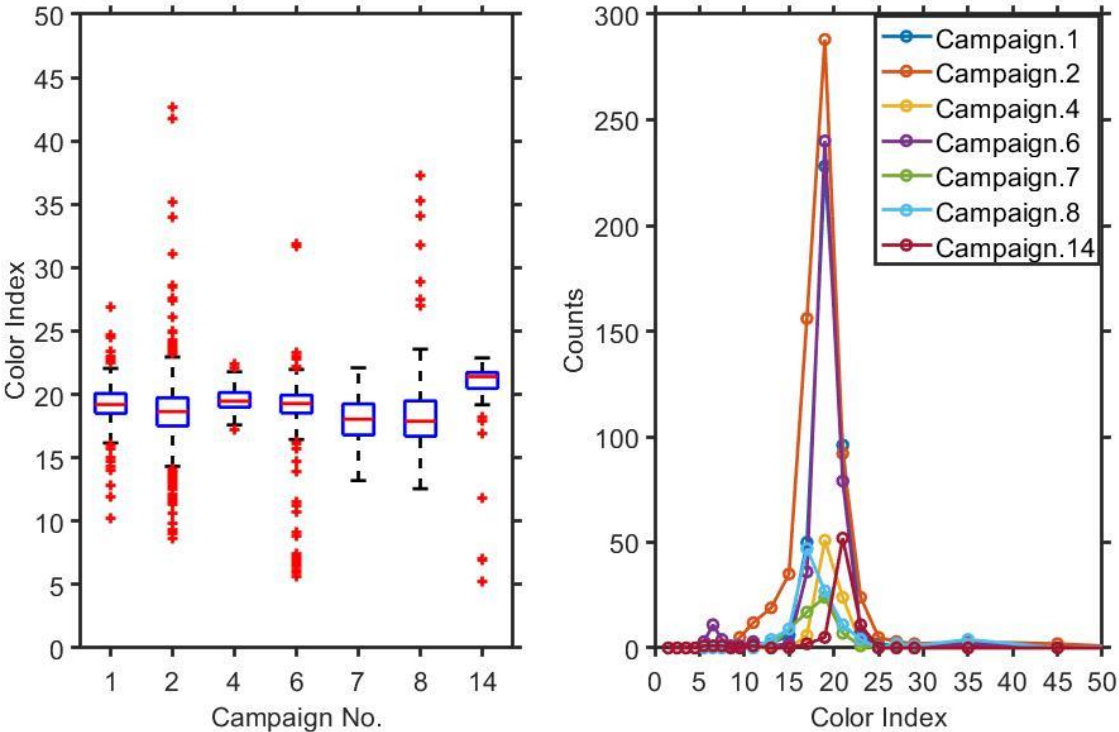
Figure 12. (a) The box plot of the Color Index (CI) was observed for the ice clouds found in different campaigns. The horizontal line in the centre of the box represents the median. The upper and lower edges of the box represent the third quartile (Q3), and first quartile (Q1) respectively. Similarly, the upper and lower whiskers represent Q3+1.5*(Q3-Q1) and Q1-1.5*(Q3-Q1). The data points beyond the whiskers (outliers) are shown with red star symbols. (b) The histogram of the CI values from each campaign. Different colours indicate the data from different campaigns.
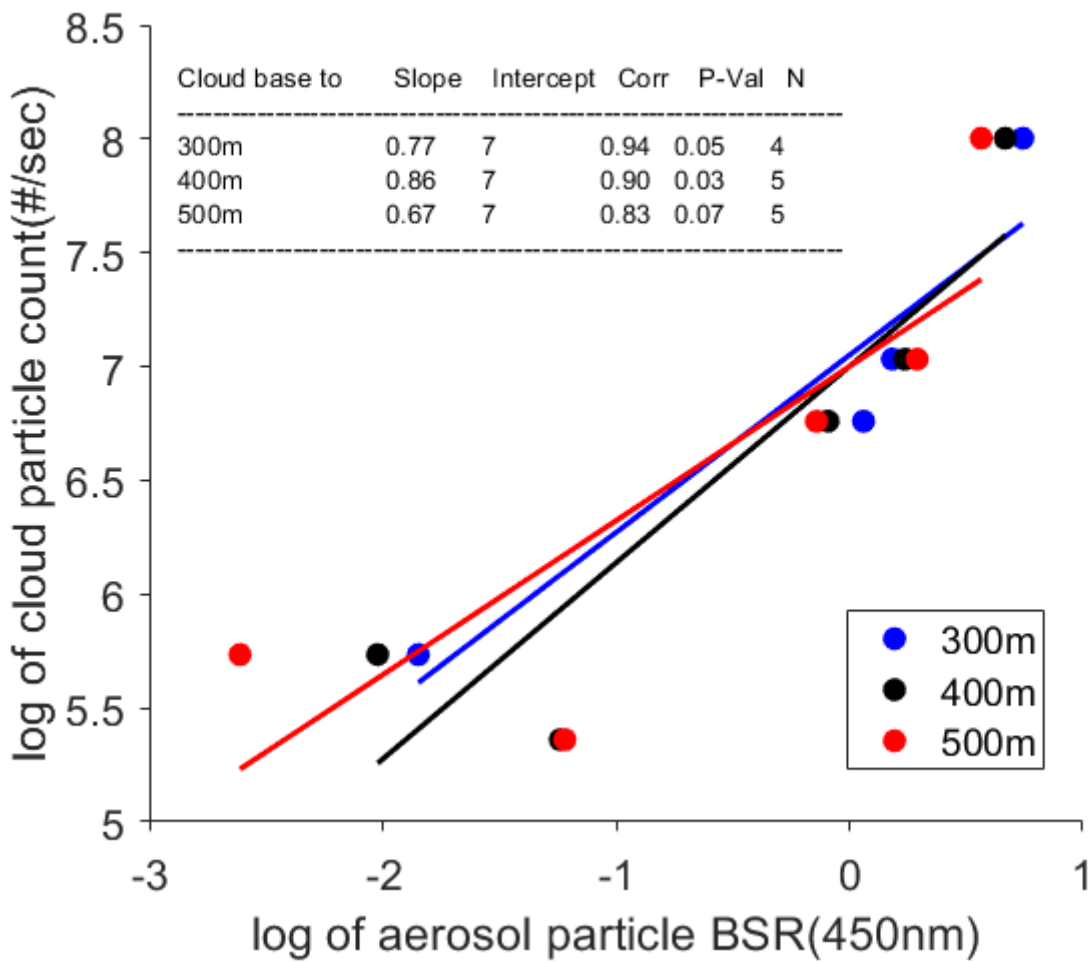
1191

1192 **Figure 13.** Scatter between logarithm values of COBALD median aerosol blue backscatter (x-axis) from 300, 400 and 500

1193 meters below the cloud base and the corresponding CPS median cloud particle count (y-axis) obtained from five balloon

1194 soundings, with a linear fit (different coloured lines). The table inside shows detailed statistics.

1195

1196

1197   *********